# High-performance multiqubit system with double-transmon couplers: Toward scalable superconducting quantum computers

Kentaro Kubo[1,*] Yinghao Ho,[1] and Hayato Goto[1,2]

[1]*Frontier Research Laboratory, Corporate Research & Development Center,* Toshiba Corporation, *1, Komukai-Toshiba-cho, Saiwai-ku, Kawasaki 212-8582, Japan*
[2]*RIKEN Center for Quantum Computing (RQC), Wako, Saitama 351-0198, Japan*

Tunable couplers in superconducting quantum computers have enabled fast and accurate two-qubit gates, with reported high fidelities over 99% in various architectures and gate-implementation schemes. However, there are few tunable couplers whose performance in multiqubit systems is clarified, except for the most widely used one: single-transmon coupler (STC). Achieving similar accuracy to isolated two-qubit systems remains challenging due to various undesirable couplings but is necessary for scalability. In this work, we numerically analyze a system of three fixed-frequency qubits coupled via two double-transmon couplers (DTCs) where nearest-neighbor qubits are highly detuned and also next-nearest-neighbor ones are nearly resonant. The DTC is a recently proposed tunable coupler, which consists of two fixed-frequency transmons coupled through a common loop with an additional Josephson junction. We find that the DTC cannot only reduce undesired residual couplings sufficiently, as well as in isolated two-qubit systems, but also enables implementations of 30-ns CZ gates and individual and simultaneous 10-ns $\pi/2$ pulses with fidelities over 99.99%. For comparison, we also investigate the system where the DTCs are replaced by the STCs. The results show that the DTC outperforms the STC in terms of both residual coupling suppression and gate accuracy in the above systems. From these results, we expect that the DTC architecture is promising for realizing high-performance, scalable superconducting quantum computers.

## I. INTRODUCTION

The advent of tunable couplers has dramatically improved the gate performance of superconducting quantum processors [1–3]. They can substantially suppress undesired residual couplings by adjusting external parameters such as magnetic flux, and also quickly strengthen the couplings to implement fast two-qubit gates.

Although various types of tunable couplers have been proposed [3–16], so far the most standard, widely used, and well-understood one is the single-transmon coupler (STC) [3]. The STC has a simple structure consisting of a frequency-tunable transmon and capacitor between qubits [3]. Several groups have reported fast and accurate (various types of) two-qubit gate implementations using an STC in isolated two-qubit systems [17–21]. Furthermore, it has been confirmed that the functionality of the STC scales

to multiqubit systems [1,2,22–25]. However, it is known that the reduction of residual couplings for highly detuned qubits (larger than qubit anharmonicities) is challenging for the STC [19–22]. For example, it has been reported that there is the so-called residual $ZZ$ coupling of $-80$ to $-60$ kHz for about 360-MHz detuned qubits [20]. Because of this drawback, a standard architecture uses the STC together with frequency-tunable qubits with a small detuning (less than qubit anharmonicities) [1–3,17,18,24,25]. However, such nearly resonant qubits tend to suffer from frequency crowding and microwave crosstalk compared to highly detuned ones. Furthermore, tunable qubits are prone to decoherence compared with fixed-frequency ones [26,27].

To overcome this disadvantage of the STC, another kind of tunable coupler named the double-transmon coupler (DTC) has recently been proposed [29], numerically investigated [30,31], and experimentally realized [32]. The DTC consists of two fixed-frequency transmons coupled through a common loop with an additional Josephson junction [29–32]. It has been numerically [29,30] and experimentally [32] demonstrated that the DTC can make the residual $ZZ$ coupling strength completely zero or negligibly small even for highly detuned qubits, which has not been achieved with STCs. Numerical

*Contact author: kentaro3.kubo@toshiba.co.jp

gate simulations using rigorous superconducting-circuit models without decoherence effect have shown that a fast CZ gate using a tunable longitudinal coupling [29,30] and a fast $\sqrt{\text{iSWAP}}$ gate using a parametric transverse coupling [30] with fidelities over 99.99% can be implemented for highly detuned fixed-frequency transmon qubits. Furthermore, in the experimental work [32], a CZ-gate fidelity of $99.92 \pm 0.01\%$ has been realized stably during 12-h measurement. This is the highest level of two-qubit gate fidelity among superconducting quantum computers ever reported. It has also been reported in Ref. [32] that the coherence times of qubits coupled via a DTC are also at the highest level as transmons ($T_1 = 228.6, 205.3\ \mu s$ and $T_2^{\mathrm{E}} = 358.9, 129.8\ \mu s$ at the idle point). These results suggest that the degradation of the coherence time due to the noise channels introduced by a DTC may be rather smaller than or at least comparable to that of conventional tunable couplers.

However, all studies of the DTC reported so far have been done only in isolated two-qubit systems [29–32] and therefore it has not been clear whether the above abilities of the DTC can be maintained in multiqubit systems like Fig. 1(a). In other words, the scalability of the DTC architecture has not been understood well, unlike the other



architectures including the STC [1,2,22–25,33–37]. Since there are additional error sources in multiqubit systems, such as unwanted interactions between nonadjacent qubits, between a qubit and a nonadjacent coupler, and between couplers, the detailed study on multiqubit systems with multiple DTCs is highly desirable.

In this paper, we numerically study the system with three qubits coupled via two DTCs as a minimal model for the above purpose [see the highlighted part in Fig. 1(a)]. As a result, we find that ZZ coupling between nearest-neighbor (NN) qubits can be reduced as in isolated two-qubit systems. Furthermore, we show that the ZZ coupling between next-nearest-neighbor (NNN) qubits and ZZZ coupling, which do not exist in isolated two-qubit systems, can also be suppressed down to about 1 kHz. We also numerically demonstrate that 30-ns CZ gates and individual and simultaneous 10-ns $\pi/2$ pulses can be implemented with fidelities over 99.99%. These results imply that the DTC works well even in multiqubit systems. Moreover, as a comparison of the above results, we also evaluate the performance of the system where the two DTCs are replaced by the two STCs. The parameters of STCs have been set based on the experiment reporting a high-performance CZ gate [20]. The results show that the DTC outperforms the STC in terms of both residual coupling suppression and gate accuracy in the above systems. Based on our findings, the main reason for the difference lies in the fact that the STC architecture typically exhibits a larger stray coupling between the NNN qubits compared to the DTC architecture (see Sec. V).

This paper is organized as follows. In Sec. II, we introduce a theoretical model of the above three-qubit system in Fig. 1 and show the present parameter setting. In Sec. III A, we show the numerical results of the ZZ and ZZZ couplings and also two-qubit and single-qubit gates (CZ gates and individual and simultaneous $\pi/2$ pulses, respectively). For the evaluation of gate performance, we use the average gate fidelities [38,39] for the three-qubit system, which can include the effects of spectator errors [23,40–46]. In Sec. IV, for comparison, we also analyze the system where the DTCs are replaced by the STCs. In Sec. V, we discuss the difference between the results of the DTCs and the STCs. Finally, we summarize our work in Sec. VI.
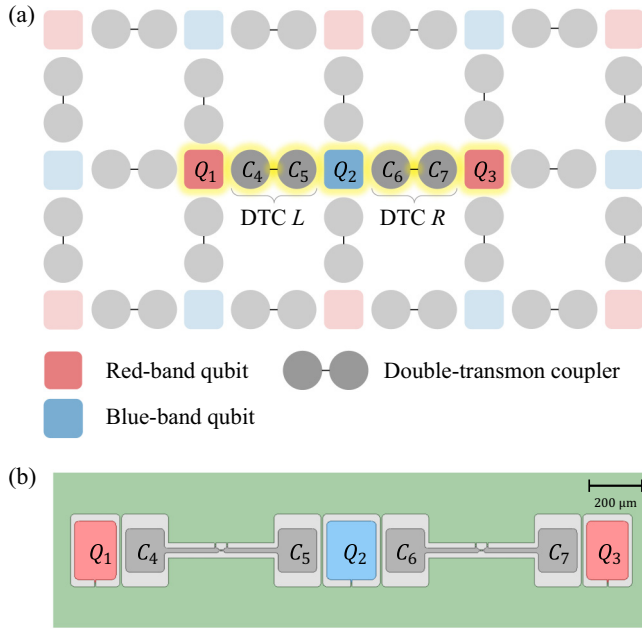
FIG. 1. (a) A typical structure of a multiqubit system with the DTCs. Squares and circles represent qubits and coupler transmons, respectively. The colors of qubits (red or blue) indicate which frequency bands (low or high) they belong to. DTCs are represented by two coupler transmons connected via a thin line. (b) A typical layout of the highlighted part of (a) corresponding to the three-qubit system that we study in this work. Its schematic circuit diagram is shown in Fig. 2(a). Its capacitances estimated by electromagnetic simulator ANSYS Q3D [28] are summarized in Table I.

## II. MODEL

### A. Circuit

We consider the three-qubit system shown by the highlighted part in Fig. 1(a). A typical device layout and a schematic circuit diagram are shown in Figs. 1(b) and 2(a), respectively. We also introduce the isolated two-qubit subsystems $L$ and $R$ shown in Figs. 2(b) and 2(c), respectively, corresponding to the left and right sides of the three-qubit system.
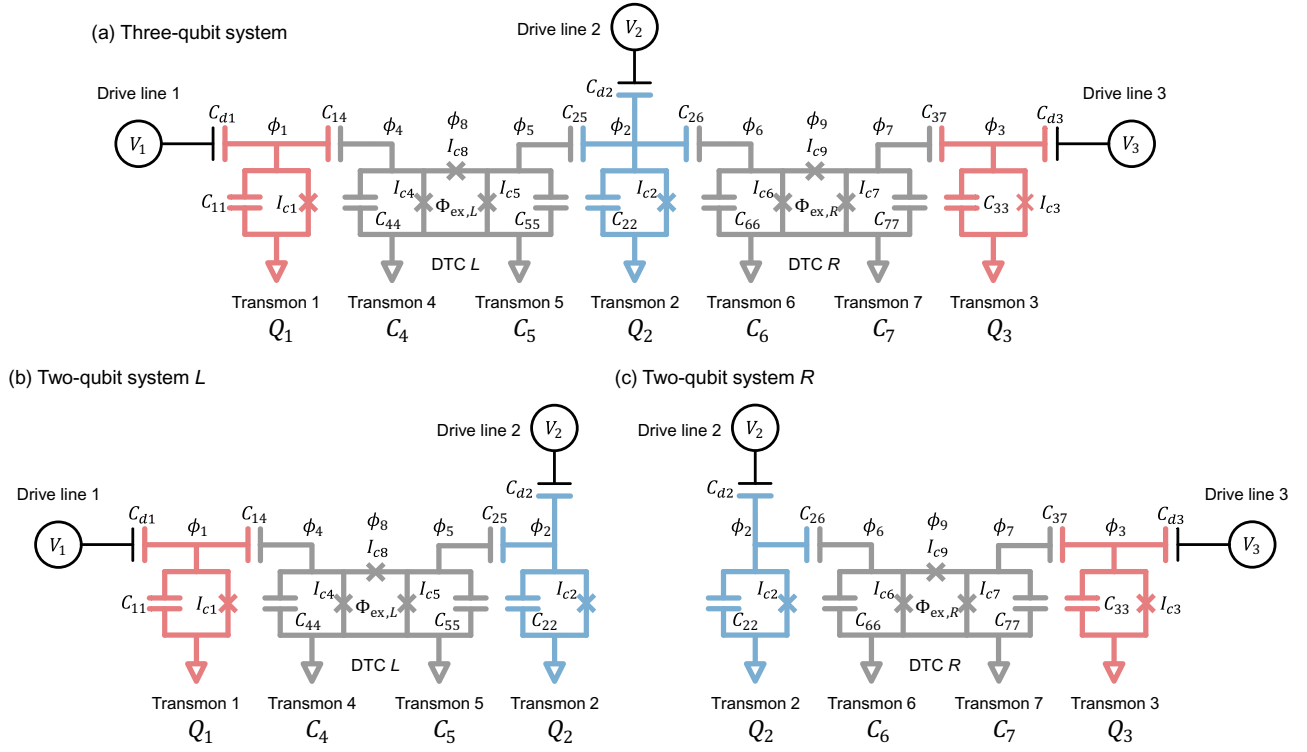
FIG. 2. (a) Circuit diagram of the three-qubit system corresponding to the highlighted part of Fig. 1. (b) Circuit diagram of the two-qubit system $L$, which is the subsystem of (a). (c) Similar diagram to (b) for the right side of (a). The colors of $Q_i$ (red or blue) indicate which frequency bands (low or high) they belong to.

The three-qubit system consists of seven transmons. Transmons 1, 2, and 3 in Fig. 2(a) are fixed-frequency qubits ($Q_1$, $Q_2$, and $Q_3$). Neighboring two-qubit pairs, $(Q_1, Q_2)$ and $(Q_2, Q_3)$, are coupled via DTCs $L$ and $R$, respectively. DTC $L$ ($R$) consists of two fixed-frequency transmons, $C_4$ and $C_5$ ($C_6$ and $C_7$), coupled through a common loop with an additional Josephson junction, the critical current of which, $I_{c8(9)}$, is smaller than that of the transmons, $I_{ci}$ ($i \in \{1, 2, 3, 4, 5, 6, 7\}$). In the loop of DTC $\mu$ ($\mu \in \{L, R\}$), the external magnetic flux $\Phi_{\mathrm{ex},\mu}$ is applied. Each qubit $Q_i$ is coupled to a drive line, where voltage $V_i$ is applied via a capacitor $C_{di}$. We assume that $C_{di}$ is negligible with respect to the other capacitances $C_{ij}$, where $C_{ii}$ is a capacitance between transmon $i$ and the ground, and $C_{ij}$ ($i \neq j$) is the one between transmons $i$ and $j$.

## B. Hamiltonian of the superconducting circuit model

We assume $V_i = 0$ except for single-qubit gates in Sec. III B 2. Then, the Hamiltonian of the rigorous circuit model of this system is written as follows (see Appendix A for the derivation):

$$\hat{H} = 4\hbar \hat{\mathbf{n}}^T W \hat{\mathbf{n}} + \left( \dot{\Theta}_{\mathrm{ex},L} \mathbf{t}_{DL}^T + \dot{\Theta}_{\mathrm{ex},R} \mathbf{t}_{DR}^T \right) \hbar W \hat{\mathbf{n}} + \hat{U}, \quad (1)$$

where

$$\hat{U} = -\sum_{i=1}^{7} \hbar \omega_{J_i} \cos \hat{\varphi}_i$$
$$- \hbar \omega_{J8} \cos(\hat{\varphi}_5 - \hat{\varphi}_4 - \Theta_{\mathrm{ex},L})$$
$$- \hbar \omega_{J9} \cos(\hat{\varphi}_7 - \hat{\varphi}_6 - \Theta_{\mathrm{ex},R}), \quad (2)$$

$$\mathbf{t}_{DL}^T = \frac{1}{\omega_{C45}} \begin{pmatrix} 0 & 0 & 0 & -1 & 1 & 0 & 0 \end{pmatrix}, \quad (3)$$

$$\mathbf{t}_{DR}^T = \frac{1}{\omega_{C67}} \begin{pmatrix} 0 & 0 & 0 & 0 & 0 & -1 & 1 \end{pmatrix}, \quad (4)$$

$\hbar$ is the reduced Planck constant, $\Theta_{\mathrm{ex},\mu} = \Phi_{\mathrm{ex},\mu}/\phi_0$ is an angle defined with the external flux $\Phi_{\mathrm{ex},\mu}$, $\phi_0 = \hbar/(2e)$ is the reduced flux quantum, $\hbar W = e^2 M^{-1}/2$ with a capacitor matrix $M$ ($M_{ii} = \sum_{j=1}^{7} C_{ij}$ and $M_{ij} = -C_{ij}$ for $i \neq j$), and $\hbar \omega_{Cij} = e^2/(2C_{ij})$ (for $i \neq j$), with the elementary charge $e$. Operators $\hat{n}_i$, $\hat{\varphi}_i$, and $\hbar \omega_{J_i} = \phi_0 I_{ci}$ are, respectively, the Cooper-pair number operator, the phase-difference operator, and the Josephson energy for the $i$th Josephson junction. Operators $\hat{n}_i$ and $\hat{\varphi}_i$ satisfy the canonical commutation relation $[\hat{\varphi}_i, \hat{n}_j] = i\delta_{i,j}$.

In numerical simulations of superconducting quantum computers, effective models derived by approximating the rigorous circuit ones are widely used [3,17–19,21–23]. The reason for this is that these models are intuitive and computationally light. However, these effective models may lead to inaccurate results compared to rigorous ones like the above. Therefore, in this study, we use the above rigorous superconducting circuit model without approximations, focusing on demonstrating the performance in an ideal situation in the absence of decoherence as rigorously as possible. In the case of a two-qubit system, it has already been reported that such simulation results are in excellent agreement with experimental ones [32].

The Hamiltonian in Eq. (1) is represented by a $(2N + 1)^7 \times (2N + 1)^7$ matrix, where $N$ is a cutoff for the Cooper-pair number (see Appendix B). In this work, we choose $N = 10$ so that the energies converge sufficiently. The matrix size of the Hamiltonian of our three-qubit system ($1801088541 \times 1801088541$) is $85766121$ times larger than the one in the two-qubit systems studied in Refs. [29,30] ($194481 \times 194481$). Note that calculations of this size are too heavy to perform in a naive manner, e.g., by directly using QuTip [47,48]. Due to these difficulties, there have been no studies that conducted gate simulations for multiqubit systems coupled via tunable coupler using rigorous circuit models, to the best of our knowledge. We overcome this difficulty introducing the dimension reduction technique in Appendix C. We have confirmed that calculated energies and gate fidelities converge with errors of the orders of sub-kHz and $10^{-5}$, respectively. Therefore, in this work we evaluate residual couplings up to 1-kHz rounding off the sub-kHz fractions and the gate fidelities up to four-digit precision rounding off the fifth decimal place.

The eigenfrequencies of the three-qubit system and corresponding eigenstates are denoted by $\omega_{Q_1,Q_2,Q_3,C_4,C_5,C_6,C_7}$ and $|Q_1, Q_2, Q_3, C_4, C_5, C_6, C_7\rangle$ ($Q_i, C_i \in 0, 1, 2, \ldots$), respectively. Since we are mainly interested in the qubit subspace, we also use notations $\omega_{Q_1,Q_2,Q_3} \equiv \omega_{Q_1,Q_2,Q_3,0,0,0,0}$ and $|Q_1, Q_2, Q_3\rangle \equiv |Q_1, Q_2, Q_3, 0, 0, 0, 0\rangle$. Hereafter, we set $\omega_{0,0,0}$ to 0.

### C. Parameter setting

Parameter settings are shown in Table I. We choose bare transmon frequencies $\omega_i$ and capacitances $C_{ij}$ as design values. By definition, $W_{ij}$ is uniquely determined by $C_{ij}$. The anharmonicity of the bare transmon $i$ is roughly given by $(-W_{ii})$ [26]. The coupling constant between the bare transmons $i$ and $j$, $g_{ij}$, is proportional to $W_{ij}$ (for $i \neq j$) as follows [29,30]:

$$g_{ij} = \frac{W_{ij}}{2} \sqrt{\frac{(\omega_i + W_{ii})(\omega_j + W_{jj})}{W_{ii} W_{jj}}}. \quad (5)$$

TABLE I. Parameter settings for the DTC circuits in Fig. 2. Bold values are design values. The others are calculated using them.

| | |
|---|---|
| $\omega_1/2\pi$ (GHz) | **5.0** |
| $\omega_2/2\pi$ (GHz) | **5.5** |
| $\omega_3/2\pi$ (GHz) | **5.01** |
| $\omega_4/2\pi$ (GHz) | **7.3** |
| $\omega_5/2\pi$ (GHz) | **7.3** |
| $\omega_6/2\pi$ (GHz) | **7.3** |
| $\omega_7/2\pi$ (GHz) | **7.3** |
| $C_{ii}$ (fF) | **80.0** |
| $C_{12}, C_{23}$ (fF) | **0.05** |
| $C_{13}$ (fF) | **0.003** |
| $C_{14}, C_{25}, C_{26}, C_{37}$ (fF) | **8.0** |
| $C_{15}, C_{24}, C_{27}, C_{36}$ (fF) | **0.1** |
| $C_{16}, C_{35}$ (fF) | **0.02** |
| $C_{17}, C_{34}$ (fF) | **0.006** |
| $C_{45}, C_{67}$ (fF) | **1.0** |
| $C_{46}, C_{57}$ (fF) | **0.05** |
| $C_{47}$ (fF) | **0.01** |
| $C_{56}$ (fF) | **1.0** |
| $I_{c1}$ (nA) | 31.0 |
| $I_{c2}$ (nA) | 40.1 |
| $I_{c3}$ (nA) | 31.1 |
| $I_{c4}$ (nA) | 65.0 |
| $I_{c5}$ (nA) | 65.2 |
| $I_{c6}$ (nA) | 65.2 |
| $I_{c7}$ (nA) | 65.0 |
| $\omega_{J1}/2\pi$ (GHz) | 15.4 |
| $\omega_{J2}/2\pi$ (GHz) | 19.9 |
| $\omega_{J3}/2\pi$ (GHz) | 15.4 |
| $\omega_{J4}/2\pi$ (GHz) | 32.3 |
| $\omega_{J5}/2\pi$ (GHz) | 32.4 |
| $\omega_{J6}/2\pi$ (GHz) | 32.4 |
| $\omega_{J7}/2\pi$ (GHz) | 32.3 |
| $r_{J8} = I_{c8}/[(I_{c4} + I_{c5})/2]$ | **0.3** |
| $r_{J9} = I_{c9}/[(I_{c6} + I_{c7})/2]$ | **0.3** |
| $I_{c8}$ (nA) | 19.5 |
| $I_{c9}$ (nA) | 19.5 |
| $\omega_{J8}/2\pi$ (GHz) | 9.69 |
| $\omega_{J9}/2\pi$ (GHz) | 9.69 |
| $W_{11}/2\pi$ (MHz) | 221 |
| $W_{22}/2\pi$ (MHz) | 204 |
| $W_{33}/2\pi$ (MHz) | 221 |
| $W_{44}/2\pi$ (MHz) | 219 |
| $W_{55}/2\pi$ (MHz) | 218 |
| $W_{66}/2\pi$ (MHz) | 218 |
| $W_{77}/2\pi$ (MHz) | 219 |
| $g_{12}/2\pi$ (MHz) | 2.34 |
| $g_{13}/2\pi$ (MHz) | 0.13 |
| $g_{14}/2\pi$ (MHz) | 283 |
| $g_{15}/2\pi$ (MHz) | 6.93 |
| $g_{16}/2\pi$ (MHz) | 1.12 |
| $g_{17}/2\pi$ (MHz) | 0.28 |
| $g_{23}/2\pi$ (MHz) | 2.35 |
| $g_{24}/2\pi$ (MHz) | 7.14 |
| $g_{25}/2\pi$ (MHz) | 284 |
| $g_{26}/2\pi$ (MHz) | 284 |
| $g_{27}/2\pi$ (MHz) | 7.14 |

TABLE I.   Continued.

| | |
|---|---|
| $g_{34}/2\pi$ (MHz) | 0.28 |
| $g_{35}/2\pi$ (MHz) | 1.12 |
| $g_{36}/2\pi$ (MHz) | 6.94 |
| $g_{37}/2\pi$ (MHz) | 283 |
| $g_{45}/2\pi$ (MHz) | 43.2 |
| $g_{46}/2\pi$ (MHz) | 3.02 |
| $g_{47}/2\pi$ (MHz) | 0.54 |
| $g_{56}/2\pi$ (MHz) | 38.8 |
| $g_{57}/2\pi$ (MHz) | 3.02 |
| $g_{67}/2\pi$ (MHz) | 43.2 |

The Josephson frequencies of transmons 1–7, $\omega_{Ji}$, are calculated as [29,30]

$$\omega_{Ji} = \frac{(\omega_i + W_{ii})^2}{8W_{ii}}. \qquad (6)$$

As for $\omega_{J8(9)}$, we set $r_{J8(9)}$, the ratio of $\omega_{J8(9)}$ to the average value of $\omega_{J4(6)}$ and $\omega_{J5(7)}$, to 0.3 [30]. The critical current $I_{ci}$ is proportional to the Josephson frequency as $I_{ci} = \hbar\omega_{Ji}/\phi_0$.

Here, we explain our parameter setting. (1) We set the detunings of the NN qubits, $(Q_1, Q_2)$ and $(Q_2, Q_3)$, to be larger than the absolute values of the qubit anharmonicities $W_{ii}$ ($i \in \{1, 2, 3\}$). Such a parameter regime, called the highly detuned regime or out-of-straddling regime [21,29], is preferable to suppress microwave crosstalk between the NN qubits, compared to the nearly resonant or in-the-straddling regime [23]. (2) From the perspective of suppressing microwave crosstalk, it is desirable to have a larger detuning between the NNN qubits $(Q_1, Q_3)$ as well. However, alternating red-band (lower-frequency) and blue-band (higher-frequency) qubits to keep the NN qubits highly detuned as shown in Fig. 1, the NNN qubits belong to the same-frequency band and thus must nearly resonate. Thus, in this work, we set the detuning between the NNN qubits to a sufficiently small value (10 MHz) compared to the anharmonicity. We will show that even with such a small detuning, crosstalk between the NNN qubits is negligible in this system, but it is not the case for the STCs. The origin of this performance difference will be discussed in Sec. V. (3) In actual circuits, there are parasitic capacitances, e.g., $C_{12}$, $C_{13}$, and $C_{56}$, which are not shown in Fig. 2. These capacitances may degrade the performance of the DTCs. Therefore, they should not be ignored. Thus, we set all of the capacitances, including the parasitic ones, to correspond to the layout shown in Fig. 1(b). We estimate them by the electromagnetic simulator ANSYS Q3D [28]. We will also discuss the case where the NNN qubits are not on the horizontal line but on the diagonal line in Appendix I. (4) We set $\omega_i$ ($i \in \{4, 5, 6, 7\}$) and $r_{Ji}$ ($i \in \{8, 9\}$) such that they lead to small residual $ZZ$ couplings and a high-performance adiabatic CZ gate operation.

## III. NUMERICAL RESULTS

### A. Idle point, $ZZ$ couplings, and $ZZZ$ coupling

Figures 3(a) and 3(b) show $\omega_{Q_1,Q_2,Q_3,C_4,C_5,C_6,C_7}$ as functions of $\Theta_{\text{ex},L(R)}$ when $\Theta_{\text{ex},R(L)}$ is fixed to $\Theta_{\text{Id},R(L)} \equiv 0.65\pi$ ($0.65\pi$). Here, $\Theta_{\text{Id},R(L)}$ is an idle point of the isolated two-qubit subsystem $L(R)$ where the $ZZ$ coupling between $Q_1$ and $Q_2$ ($Q_2$ and $Q_3$) is the closest to 0 (see Appendix D for the details). At the end of this subsection, we will explain the validity that the idle point of the three-qubit system can be chosen as $(\Theta_{\text{ex},L}, \Theta_{\text{ex},R}) = (\Theta_{\text{Id},L}, \Theta_{\text{Id},R})$. The qubit frequencies of the three-qubit system, $\omega_{Q_1,Q_2,Q_3}$ ($Q_i \in \{0, 1\}$), are highlighted by being colored and bold, and the ones of the two-qubit system, $\omega^\mu_{Q_i,Q_j}$ ($Q_i, Q_j \in \{0, 1\}$ and $\mu \in \{L, R\}$) (see Appendix D), are shown by scatter plots. All of them are needed for calculations of $ZZ$ and $ZZZ$ couplings below. We find that $\omega_{1,0,0}$, $\omega_{0,1,0}$, $\omega_{0,0,1}$, $\omega_{1,1,0}$, and $\omega_{0,1,1}$ are in good agreement with the corresponding ones in the two-qubit systems. The black thin curves are frequencies of the states other than the computational state. They cannot be ignored to account for leakage errors during gate simulations.

The $ZZ$ coupling between $Q_i$ and $Q_j$ is denoted by $\zeta_{ij}$ ($i < j$). The ones between the NN qubits, $\zeta_{12}$ and $\zeta_{23}$, are expressed as follows in the three-qubit system:

$$\zeta_{12} = \omega_{1,1,0} - \omega_{1,0,0} - \omega_{0,1,0} + \omega_{0,0,0}, \qquad (7)$$

$$\zeta_{23} = \omega_{0,1,1} - \omega_{0,1,0} - \omega_{0,0,1} + \omega_{0,0,0}. \qquad (8)$$

We use the same notation, $\zeta_{12}$ and $\zeta_{23}$, for the corresponding $ZZ$ couplings in systems $L$ and $R$, respectively (see Appendix D for their definitions). The scatter plot in Figs. 3(c) and 3(d) show $\zeta_{12(23)}$ in system $L(R)$. The above $\Theta_{\text{Id},L(R)}$ has been identified as the point where $|\zeta_{12(23)}|$ takes the smallest value. We find that $\zeta_{12(23)}$ in the three-qubit system as a function of $\Theta_{\text{ex},L(R)}$ [the blue (orange) curve] is in good agreement with the one in system $L(R)$. We also found that $\zeta_{23(12)}$ is almost independent of $\Theta_{\text{ex},L(R)}$ in the three-qubit system and its value is close to the one at the idle point in the isolated two-qubit system $R(L)$ shown by the dotted horizontal line in Figs. 3(c) and 3(d). This independence is reasonable because $\Theta_{\text{ex},L(R)}$ is the parameter of DTC $L(R)$ only connecting $Q_1$ and $Q_2$ ($Q_2$ and $Q_3$).

So far, we have considered $ZZ$ coupling between NN qubits, which also exists in two-qubit subsystems. Here, we consider the $ZZ$ coupling between the NNN qubits $\zeta_{13}$ and the $ZZZ$ coupling, which exist only in $n(\geq 3)$-qubit systems. In the three-qubit system, they are expressed as follows:

$$\zeta_{13} = \omega_{1,0,1} - \omega_{1,0,0} - \omega_{0,0,1} + \omega_{0,0,0}, \qquad (9)$$

$$\zeta_{ZZZ} = \omega_{1,1,1} - [\omega_{1,0,0} + \omega_{0,1,0} + \omega_{0,0,1}]$$
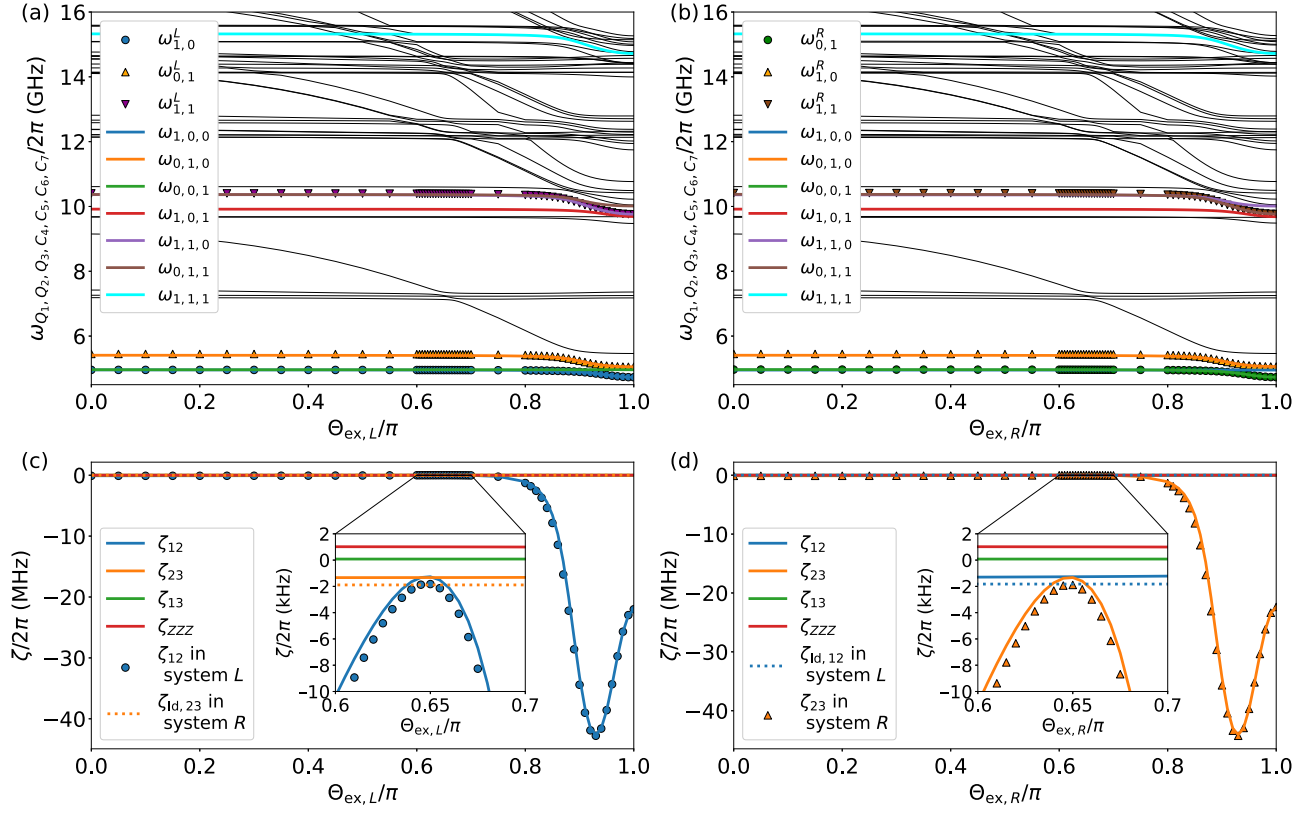$$- [\zeta_{12} + \zeta_{13} + \zeta_{23}] + 2\omega_{0,0,0}. \qquad (10)$$

FIG. 3. Energy levels and $ZZ$ coupling strengths of the systems in Fig. 2. (a),(b) show eigenfrequencies $\omega_{Q_1,Q_2,Q_3,C_4,C_5,C_6,C_7}$ as functions of $\Theta_{\mathrm{ex},L}$ and $\Theta_{\mathrm{ex},R}$, respectively. The qubit frequencies of the three-qubit system, $\omega_{Q_1,Q_2,Q_3}$ ($Q_i \in \{0,1\}$), are highlighted by being colored and bold, and the ones of the two-qubit system, $\omega^{\mu}_{Q_i,Q_j}$ ($Q_i, Q_j \in \{0,1\}$ and $\mu \in \{L,R\}$) (see Appendix D), are shown by colored scatter plots. Eigenfrequencies $\omega_{Q_1,Q_2,Q_3,C_4,C_5,C_6,C_7}$ other than the above are represented by black thin curves. (c),(d) represent $ZZ$ and $ZZZ$ couplings as functions of $\Theta_{\mathrm{ex},L}$ and $\Theta_{\mathrm{ex},R}$, respectively. Solid curves represent the ones of the three-qubit system, and scatter plots represent $\zeta_{12(23)}$ in the system $L(R)$. The orange (blue) dotted horizontal line is $\zeta_{\mathrm{Id},23(12)}$ in the system $R(L)$. Note that $\Theta_{\mathrm{ex},R}$ in the left column and $\Theta_{\mathrm{ex},L}$ in the right column are fixed to $\Theta_{\mathrm{Id},R}$ and $\Theta_{\mathrm{Id},L}$, respectively.

From Figs. 3(c) and 3(d), we found that $|\zeta_{13}|$ and $|\zeta_{ZZZ}|$ take negligibly small values of about 0–1 kHz in the wide range of the external flux.

Thus, we conclude that $\zeta_{12}$ and $\zeta_{23}$ are almost unchanged from the ones of the isolated two-qubit systems and also $\zeta_{13}$ and $\zeta_{ZZZ}$ are negligible. Therefore, it is reasonable to take the idle point of the three-qubit system to $(\Theta_{\mathrm{ex},L}, \Theta_{\mathrm{ex},R}) = (\Theta_{\mathrm{Id},L}, \Theta_{\mathrm{Id},R})$, as mentioned above. We represent $\zeta_{12}$, $\zeta_{23}$, $\zeta_{13}$, and $\zeta_{ZZZ}$ at the idle point simply as $\zeta_{\mathrm{Id},12}$, $\zeta_{\mathrm{Id},23}$, $\zeta_{\mathrm{Id,13}}$, and $\zeta_{\mathrm{Id},ZZZ}$, respectively. Their values are summarized in Table II.

### B. Gate performance

To evaluate gate performance, we calculate an average gate fidelity $\bar{F}$. This is defined by averaging gate fidelities over uniformly distributed initial states and calculated by the following formula [38,39]:

$$\bar{F} = \frac{\left|\mathrm{tr}(\hat{U}^{\dagger}_{\mathrm{id}}\hat{U}')\right|^2 + \mathrm{tr}\left(\hat{U}'^{\dagger}\hat{U}'\right)}{d(d+1)}, \qquad (11)$$

where $d = 2^n$ for an $n$-qubit system, $\hat{U}_{\mathrm{id}}$ is an ideal (target) gate operation matrix, and $\hat{U}'$ is an implemented gate operation matrix determined by numerical results (see Appendices E and F).

#### 1. Two-qubit gate: CZ gate

We aim to implement 30-ns CZ gates for qubit pairs $(Q_1, Q_2)$ and $(Q_2, Q_3)$. Their $\hat{U}_{\mathrm{id}}$ in the three-qubit system

TABLE II. Residual $ZZ$ couplings and $ZZZ$ coupling in the DTC architecture.

| | $\zeta_{\mathrm{Id},12}/(2\pi)$ | $\zeta_{\mathrm{Id},23}/(2\pi)$ | $\zeta_{\mathrm{Id},13}/(2\pi)$ | $\zeta_{\mathrm{Id},ZZZ}/(2\pi)$ |
|---|---|---|---|---|
| Three-qubit system | $-1$ kHz | $-1$ kHz | $0$ kHz | $1$ kHz |
| Two-qubit system | $-2$ kHz | $-2$ kHz | N/A | N/A |

TABLE III. Average gate fidelities of 30-ns CZ gates and 10-ns individual and simultaneous $\pi/2$ pulses. They are implemented by optimized pulses in the DTC architecture.

| Average gate fidelity (%) | $\bar{F}_{\text{CZ},12}$ | $\bar{F}_{\text{CZ},23}$ | $\bar{F}_{\pi/2,\{1\}}$ | $\bar{F}_{\pi/2,\{2\}}$ | $\bar{F}_{\pi/2,\{3\}}$ | $\bar{F}_{\pi/2,\{1,2\}}$ | $\bar{F}_{\pi/2,\{2,3\}}$ | $\bar{F}_{\pi/2,\{1,3\}}$ | $\bar{F}_{\pi/2,\{1,2,3\}}$ |
|---|---|---|---|---|---|---|---|---|---|
| Three-qubit system | 100.00 | 100.00 | 100.00 | 100.00 | 100.00 | 100.00 | 100.00 | 100.00 | 100.00 |
| Two-qubit system | 100.00 | 100.00 | ... | ... | ... | ... | ... | ... | ... |

are given as follows:

$$\hat{U}_{\text{CZ},12} = \hat{U}_{\text{CZ}} \otimes \hat{I}, \tag{12}$$

$$\hat{U}_{\text{CZ},23} = \hat{I} \otimes \hat{U}_{\text{CZ}}, \tag{13}$$

where $\hat{U}_{\text{CZ}} = \text{diag}(1, 1, 1, -1)$ and $\hat{I}$ is the $2 \times 2$ identity matrix. In two-qubit subsystems $L$ and $R$, $\hat{U}_{\text{CZ},12}$ and $\hat{U}_{\text{CZ},23}$ are simply $\hat{U}_{\text{CZ}}$. In the following, the average gate fidelities of $\hat{U}_{\text{CZ},12}$ and $\hat{U}_{\text{CZ},23}$ are denoted by $\bar{F}_{\text{CZ},12}$ and $\bar{F}_{\text{CZ},23}$, respectively.

To implement $\hat{U}_{\text{CZ},12(23)}$ in the three-qubit system, we fix $\Theta_{\text{ex},R(L)}$ to $\Theta_{\text{Id},R(L)}$ and apply a optimized flux pulse $\Theta_{\text{ex},L(R)}(t)$ (see Appendix G 1). We can successfully implement 30-ns CZ gates with average fidelities over 99.99% for both qubit pairs, as summarized in Table III. Comparing these fidelities with the corresponding ones in the isolated two-qubit subsystems, we find that the degradation of the CZ gate fidelity due to the increasing number of qubits from two to three is negligible in the four-digit precision.

### 2. Single-qubit gate: $\pi/2$ pulse

Next, we consider the single-qubit gate as well. Our targets are individual and simultaneous implementations of 10-ns $\pi/2$ pulses. It leads to the following $\hat{U}_{\text{id}}$:

$$\hat{U}_{\pi/2,\{1\}} = \hat{U}_{\pi/2} \otimes \hat{I} \otimes \hat{I}, \tag{14}$$

$$\hat{U}_{\pi/2,\{2\}} = \hat{I} \otimes \hat{U}_{\pi/2} \otimes \hat{I}, \tag{15}$$

$$\hat{U}_{\pi/2,\{3\}} = \hat{I} \otimes \hat{I} \otimes \hat{U}_{\pi/2}, \tag{16}$$

$$\hat{U}_{\pi/2,\{1,2\}} = \hat{U}_{\pi/2} \otimes \hat{U}_{\pi/2} \otimes \hat{I}, \tag{17}$$

$$\hat{U}_{\pi/2,\{2,3\}} = \hat{I} \otimes \hat{U}_{\pi/2} \otimes \hat{U}_{\pi/2}, \tag{18}$$

$$\hat{U}_{\pi/2,\{1,3\}} = \hat{U}_{\pi/2} \otimes \hat{I} \otimes \hat{U}_{\pi/2}, \tag{19}$$

$$\hat{U}_{\pi/2,\{1,2,3\}} = \hat{U}_{\pi/2} \otimes \hat{U}_{\pi/2} \otimes \hat{U}_{\pi/2}, \tag{20}$$

where

$$\hat{U}_{\pi/2} = \frac{1}{\sqrt{2}} \begin{pmatrix} 1 & -i \\ -i & 1 \end{pmatrix}. \tag{21}$$

The average gate fidelity of $\hat{U}_{\pi/2,k}$ is denoted by $\bar{F}_{\pi/2,k}$ for $k \in \{\{1\}, \{2\}, \{3\}, \{1, 2\}, \{2, 3\}, \{1, 3\}, \{1, 2, 3\}\}$.

To implement $\hat{U}_{\pi/2,k}$, we fix $\Theta_{\text{ex},\mu}$ to $\Theta_{\text{Id},\mu}$ and apply a driving voltage to $Q_i$ for $i \in k$. This operation is described by the following Hamiltonian (see Appendix A for the derivation):

$$\hat{H}_V = 4\hbar \hat{\mathbf{n}}^T W \hat{\mathbf{n}} + \sum_{i \in k} \alpha_i \sum_{j=1}^{7} \hbar W_{ij} \hat{n}_j + \hat{U}(\Theta_{\text{Id},L}, \Theta_{\text{Id},R}), \tag{22}$$

where $\alpha_i$ is a dimensionless parameter controlled by $V_i$ (see Appendix A). Applying optimized $\alpha_i(t)$ (see Appendix G 2), we can implement individual and simultaneous 10-ns $\pi/2$ pulses with average gate fidelities over 99.99% as summarized in Table III.

In this section, we have shown that DTCs cannot only reduce undesired residual couplings to several kHz but also enable implementations of fast CZ gates and individual and simultaneous $\pi/2$ pulses with average fidelities over 99.99%, in the three-qubit system as well as in isolated two-qubit systems. These results indicate that the DTC architecture is scalable for highly detuned fixed-frequency qubits.

## IV. COMPARISON WITH STC ARCHITECTURE

For comparison, here we consider the system where the DTCs in Fig. 2(a) are replaced by STCs. We compare the DTC architecture with the STC one with respect to the following:

1.  Residual $ZZ$ and $ZZZ$ couplings.
2.  Average gate fidelities of optimized 30-ns CZ gates and of optimized 10-ns $\pi/2$ pulses.

### A. Circuit

The circuit diagram is shown in Fig. 4(a). This system consists of five transmons. STC $L$ ($R$) consists of a tunable-frequency transmon $C_4$ ($C_5$) and a capacitor $C_{12}$ ($C_{23}$). The tunable-frequency transmon $C_i$ ($i \in \{4, 5\}$) consists of two capacitors, $C_{iiA}$ and $C_{iiB}$, and a dc SQUID including two Josephson junctions with critical currents $I_{ciA}$ and $I_{ciB}$. Operator $\hat{\varphi}_{iv}$ and $\hbar\omega_{Jiv} = \phi_0 I_{civ}$ are, respectively, the phase-difference operator and the Josephson energy corresponding to $I_{civ}$ ($v \in \{A, B\}$). In the following, we assume $C_{iiA} = C_{iiB}$ and use notations $C_{ii} = C_{iiA} + C_{iiB}$, $I_{ci} = I_{ciA} + I_{ciB}$, and $\omega_{Ji} = \omega_{JiA} + \omega_{JiB}$.

## B. Hamiltonian of the superconducting circuit model

We assume $V_i = 0$ except for single-qubit gates. The Hamiltonian of this system is then written as follows (see Appendix A for the derivation):

$$\hat{H} = 4\hbar \hat{\mathbf{n}}^T W \hat{\mathbf{n}} + \left( \dot{\Theta}_{\mathrm{ex},L} \mathbf{t}_{SL}^T + \dot{\Theta}_{\mathrm{ex},R} \mathbf{t}_{SR}^T \right) \hbar W \hat{\mathbf{n}} + \hat{U}, \quad (23)$$

$$\begin{aligned}
\hat{U} = &- \sum_{i=1}^{3} \hbar\omega_{Ji} \cos(\hat{\varphi}_i) \\
&- \left[ \hbar\omega_{J4A} + \hbar\omega_{J4B} \cos(\Theta_{\mathrm{ex},L}) \right] \cos(\hat{\varphi}_4) \\
&- \hbar\omega_{J4B} \sin(\Theta_{\mathrm{ex},L}) \sin(\hat{\varphi}_4) \\
&- \left[ \hbar\omega_{J5A} + \hbar\omega_{J5B} \cos(\Theta_{\mathrm{ex},R}) \right] \cos(\hat{\varphi}_5) \\
&- \hbar\omega_{J5B} \sin(\Theta_{\mathrm{ex},R}) \sin(\hat{\varphi}_5),
\end{aligned} \quad (24)$$

where $\hbar W = e^2 M^{-1}/2$ with a capacitor matrix $M$ ($M_{ii} = \sum_{j=1}^{5} C_{ij}$ and $M_{ij} = -C_{ij}$ for $i \neq j$),

$$\mathbf{t}_{SL}^T = \frac{1}{2} \left( -\frac{1}{\omega_{C14}} \quad -\frac{1}{\omega_{C24}} \quad -\frac{1}{\omega_{C34}} \quad \sum_{i=1}^{5} \frac{1}{\omega_{Ci4}} \quad -\frac{1}{\omega_{C45}} \right), \quad (25)$$

$$\mathbf{t}_{SR}^T = \frac{1}{2} \left( -\frac{1}{\omega_{C15}} \quad -\frac{1}{\omega_{C25}} \quad -\frac{1}{\omega_{C35}} \quad -\frac{1}{\omega_{C45}} \quad \sum_{i=1}^{5} \frac{1}{\omega_{Ci5}} \right), \quad (26)$$

and we have removed $\hat{\varphi}_{4B(5B)}$ using the constraint $\phi_{4B(5B)} = \phi_{4A(5A)} - \Phi_{\mathrm{ex},L(R)}$ and simply written $\hat{\varphi}_{4A(5A)}$ as $\hat{\varphi}_{4(5)}$. The matrix representation of the Hamiltonian can be obtained in the same manner as the DTC architecture. We again choose the Cooper-pair number cutoff $N = 10$ for sufficient convergence of energies.

The eigenfrequencies of the three-qubit system and corresponding eigenstates are denoted by $\omega_{Q_1,Q_2,Q_3,C_4,C_5}$ and $|Q_1, Q_2, Q_3, C_4, C_5\rangle$ ($Q_i, C_i \in 0, 1, 2, \ldots$), respectively. Similarly to the DTCs, we also use notations of qubit frequencies $\omega_{Q_1,Q_2,Q_3} \equiv \omega_{Q_1,Q_2,Q_3,0,0}$ and the corresponding eigenstates $|Q_1, Q_2, Q_3\rangle \equiv |Q_1, Q_2, Q_3, 0, 0\rangle$.

Note that almost all previous theoretical analyses of the STC reported in the literature have been based on the effective model [3,17–19,21–23]. Unlike them, we use the circuit model for higher accuracy, as well as the DTCs. To the best of our knowledge, this is the first estimation of $ZZ$ coupling between NNN qubits and $ZZZ$ coupling and also the first gate simulation based on the circuit model for systems with the STCs.
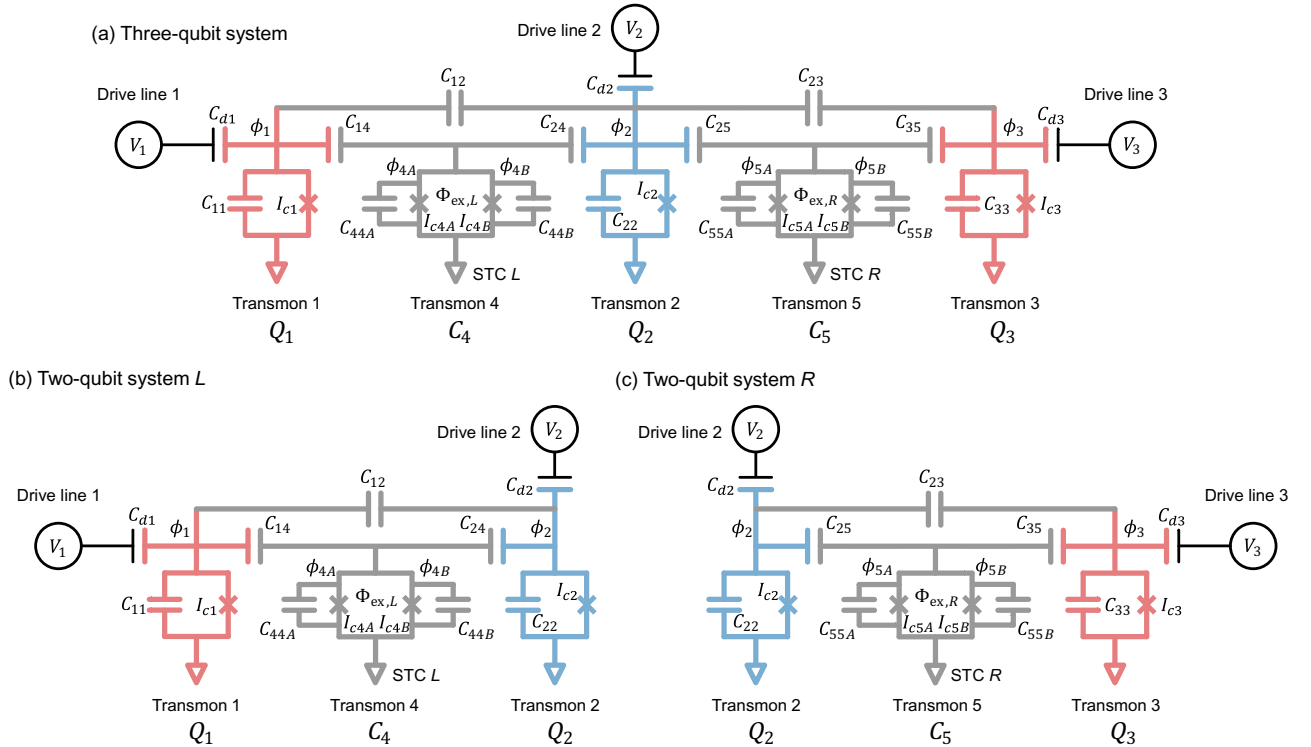


FIG. 4. (a) Circuit diagram of the system with three qubits coupled via two STCs. (b) Circuit diagram of the two-qubit system $L$, which is the subsystem of (a). (c) Similar diagram to (b) for the right side of (a). The colors of $Q_i$ (red or blue) indicate which frequency bands (low or high) they belong to.
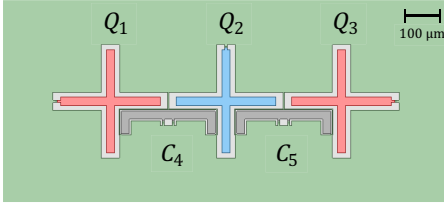
FIG. 5. The scaled-up design of the circuit in Ref. [20]. Its capacitances estimated by electromagnetic simulator ANSYS Q3D [28] are summarized in Table IV.

### C. Comparing conditions

The preferable parameter setting for the comparison between the STC and DTC architectures is nontrivial. This is because the STC and the DTC obey different operating principles, resulting in different parameter values desired for high performance. Here, in order to make the comparison as fair as possible, we set the parameters as shown in Table IV, considering the following points. (1) We set $\omega_i$ and $C_{ii}$ for $i \in \{1, 2, 3\}$ to be the same as in Table I, which means that qubit frequencies and anharmonicities are almost the same as in the DTC case. (2) Under this condition, we set $C_{ij}$ that exists in the two-qubit subsystems and $I_{c4B(c5B)}/I_{c4A(c5A)}$ to the almost same values as the corresponding ones in Ref. [20], and we also set $\omega_{4(5)}$ to the almost same value as the coupler idle frequency in Ref. [20]. Reference [20] experimentally implemented a high-performance CZ gate (with a gate time of 38 ns and a fidelity of 97.9%), using a parameter setting close to the above condition (1), where qubit frequencies are 5.038 and 5.400 GHz and both qubit capacitances are 77.8 fF. Moreover, they also showed that the magnitude of the residual *ZZ* coupling can be suppressed to 60–80 kHz by an STC, which is known to be one of the most *ZZ*-coupling suppressed results for highly detuned qubits where a fast CZ gate can be implemented. We will show that our numerical simulation reproduces their results well. (3) As for the rest $C_{ij}$ that does not exist in the two-qubit subsystems (e.g., $C_{13}$, $C_{15}$, and $C_{45}$), we choose feasible values estimated by electromagnetic simulator ANSYS Q3D [28] assuming the scaled-up design of the circuit in Ref. [20] (see Fig. 5).

### D. Numerical results

#### 1. Idle point, ZZ couplings, and ZZZ coupling

Figures 6(a) and 6(b) show $\omega_{Q_1,Q_2,Q_3,C_4,C_5}$ as functions of $\Theta_{\text{ex},L(R)}$ when $\Theta_{\text{ex},R(L)}$ is fixed to the idle point of the isolated two-qubit subsystems $L(R)$ $\Theta_{\text{Id},R(L)} \equiv 0(0)$ (see Appendix D). The qubit frequencies of the three-qubit system, $\omega_{Q_1,Q_2,Q_3}$ ($Q_i \in \{0, 1\}$), are highlighted by being colored and bold, and the ones of the two-qubit system,

TABLE IV. Parameter setting for the STC circuits in Fig. 4. Bold values are design values. The others are calculated using them.

| | |
|---|---:|
| $\omega_1/(2\pi)$ (GHz) | **5.0** |
| $\omega_2/(2\pi)$ (GHz) | **5.5** |
| $\omega_3/(2\pi)$ (GHz) | **5.01** |
| $\omega_4/(2\pi)$ (GHz) | **7.7** |
| $\omega_5/(2\pi)$ (GHz) | **7.7** |
| $C_{ii}$ (fF) for $i \in \{1, 2, 3\}$ | **80.0** |
| $C_{iiA}$, $C_{iiB}$ (fF) | **30.0** |
| $C_{12}$, $C_{23}$ (fF) | **0.5** |
| $C_{13}$ (fF) | **0.03** |
| $C_{14}$, $C_{24}$, $C_{25}$, $C_{35}$ (fF) | **6.5** |
| $C_{15}$, $C_{34}$ (fF) | **0.05** |
| $C_{45}$ (fF) | **0.25** |
| $I_{c1}$ (nA) | 30.7 |
| $I_{c2}$ (nA) | 39.3 |
| $I_{c3}$ (nA) | 30.8 |
| $\omega_{J1}/(2\pi)$ (GHz) | 15.2 |
| $\omega_{J2}/(2\pi)$ (GHz) | 19.5 |
| $\omega_{J3}/(2\pi)$ (GHz) | 15.3 |
| $I_{ciB}/I_{ciA}$ | **1/1.71** |
| $I_{ciA}$ (nA) | 37.7 |
| $I_{ciB}$ (nA) | 22.0 |
| $\omega_{JiA}/(2\pi)$ (GHz) | 18.7 |
| $\omega_{JiB}/(2\pi)$ (GHz) | 10.9 |
| $W_{11}/2\pi$ (MHz) | 224 |
| $W_{22}/2\pi$ (MHz) | 209 |
| $W_{33}/2\pi$ (MHz) | 224 |
| $W_{44}/2\pi$ (MHz) | 268 |
| $W_{55}/2\pi$ (MHz) | 268 |
| $g_{12}/2\pi$ (MHz) | 33.0 |
| $g_{13}/2\pi$ (MHz) | 1.62 |
| $g_{14}/2\pi$ (MHz) | 265 |
| $g_{15}/2\pi$ (MHz) | 6.13 |
| $g_{23}/2\pi$ (MHz) | 33.0 |
| $g_{24}/2\pi$ (MHz) | 268 |
| $g_{25}/2\pi$ (MHz) | 268 |
| $g_{34}/2\pi$ (MHz) | 6.14 |
| $g_{35}/2\pi$ (MHz) | 265 |
| $g_{45}/2\pi$ (MHz) | 39.2 |

$\omega_{Q_i,Q_j}^{\mu}$ ($Q_i, Q_j \in \{0, 1\}$ and $\mu \in \{L, R\}$) are shown by scatter plots. All of them are needed for calculations of *ZZ* and *ZZZ* couplings below. Similarly to the DTC architecture, we find that the corresponding qubit frequencies of the three-qubit and two-qubit systems are in good agreement with each other. The black thin curves represent the states other than the computational ones. They are necessary for accounting leakage errors during gate simulations.

Figures 6(c) and 6(d) show the *ZZ* and *ZZZ* couplings. Solid curves represent the ones of the three-qubit system, and scatter plots represent the ones of the two-qubit system. We find that $\zeta_{12}$ and $\zeta_{23}$, are almost unchanged from
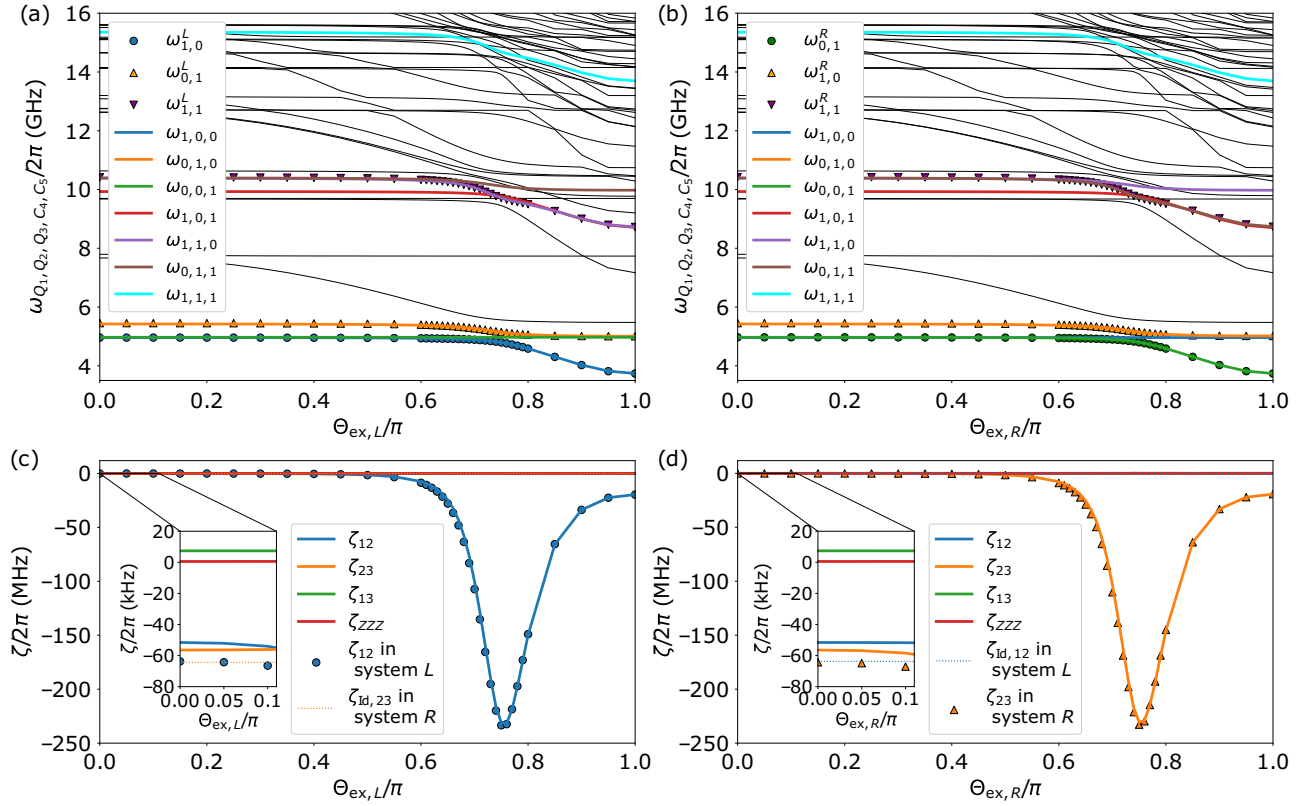
FIG. 6. Energy levels and *ZZ* coupling strengths of the systems in Fig. 4. (a),(b) show eigenfrequencies $\omega_{Q_1,Q_2,Q_3,C_4,C_5}$ as functions of $\Theta_{\text{ex},L}$ and $\Theta_{\text{ex},R}$, respectively. The qubit frequencies of the three-qubit system, $\omega_{Q_1,Q_2,Q_3}$ ($Q_i \in \{0,1\}$), are highlighted by being colored and bold, and the ones of the two-qubit system, $\omega_{Q_i,Q_j}^{\mu}$ ($Q_i, Q_j \in \{0,1\}$ and $\mu \in \{L,R\}$) (see Appendix D), are shown by colored scatter plots. Eigenfrequencies $\omega_{Q_1,Q_2,Q_3,C_4,C_5}$ other than the above are represented by black thin curves. (c),(d) represent *ZZ* and *ZZZ* couplings as functions of $\Theta_{\text{ex},L}$ and $\Theta_{\text{ex},R}$, respectively. Solid curves represent the ones of the three-qubit system, and scatter plots represent $\zeta_{12(23)}$ in the system $L(R)$. The orange (blue) dotted horizontal line is $\zeta_{\text{Id},23(12)}$ in the system $R(L)$. Note that $\Theta_{\text{ex},R}$ in the left column and $\Theta_{\text{ex},L}$ in the right column are fixed to $\Theta_{\text{Id},R}$ and $\Theta_{\text{Id},L}$, respectively.

the ones of the isolated two-qubit systems and $\zeta_{13}$ and $\zeta_{ZZZ}$ are negligibly small (about 10 and 0 kHz, respectively). These results show that STCs can suppress the residual couplings even in three-qubit systems. Therefore, we can take the idle point of the three-qubit system to $(\Theta_{\text{ex},L}, \Theta_{\text{ex},R}) = (\Theta_{\text{Id},L}, \Theta_{\text{Id},R})$. However, as in the two-qubit system, their magnitudes shown in Table V are about an order of magnitude larger than the corresponding ones of the DTC architecture. These results show that the DTC is superior to the STC in terms of the residual couplings in three-qubit systems, as well as in two-qubit systems.

### 2. Gate performance

Gate simulation results are summarized in Table VI. We find that 30-ns CZ gates with average fidelities of 99.99% cannot be achieved in the three-qubit system. This is in contrast to the corresponding fidelities of the two-qubit subsystems, which exceeds 99.99%. The fidelity degradation of the CZ gate due to the scaleup from two qubits to three is about 0.2%–0.6%, which is roughly 10 times larger than the corresponding one in the DTC architecture. We also find that 10-ns $\pi/2$ pulses with average fidelities over 99.99% cannot be implemented except for $Q_2$. The infidelities of the $\pi/2$ pulses for $Q_1$ and $Q_3$, are about 0.2%.

TABLE V.    Residual *ZZ* couplings and *ZZZ* coupling in the STC architecture.

| | $\zeta_{\text{Id},12}/(2\pi)$ | $\zeta_{\text{Id},23}/(2\pi)$ | $\zeta_{\text{Id},13}/(2\pi)$ | $\zeta_{\text{Id},ZZZ}/(2\pi)$ |
|---|---|---|---|---|
| Three-qubit system | −52 kHz | −56 kHz | 8 kHz | 1 kHz |
| Two-qubit system | −64 kHz | −64 kHz | N/A | N/A |

TABLE VI. Average gate fidelities of 30-ns CZ gates and 10-ns individual and simultaneous $\pi/2$ pulses. They are implemented by optimized pulses in the STC architecture.

| Average gate fidelity (%) | $\bar{F}_{\text{CZ},12}$ | $\bar{F}_{\text{CZ},23}$ | $\bar{F}_{\pi/2,\{1\}}$ | $\bar{F}_{\pi/2,\{2\}}$ | $\bar{F}_{\pi/2,\{3\}}$ | $\bar{F}_{\pi/2,\{1,2\}}$ | $\bar{F}_{\pi/2,\{2,3\}}$ | $\bar{F}_{\pi/2,\{1,3\}}$ | $\bar{F}_{\pi/2,\{1,2,3\}}$ |
|---|---|---|---|---|---|---|---|---|---|
| Three-qubit system | 99.81 | 99.38 | 99.80 | 100.00 | 99.79 | 99.80 | 99.79 | 99.63 | 99.62 |
| Two-qubit system | 100.00 | 100.00 | ... | ... | ... | ... | ... | ... | ... |

This is also roughly 10 times larger than the corresponding ones of the system of the DTC.

From these results, we conclude that the DTC exhibits higher scalability than the STC, as the tunable coupler for highly detuned fixed-frequency qubits.

## V. DISCUSSION

As demonstrated in the above two sections, the DTCs can implement more accurate gate operations in the three-qubit system than the STCs. This difference mainly comes from the larger parasitic coupling of the NNN qubits $g_{13}$ in the STC architecture than that in the DTC architecture (see Tables I and IV). Since tunable couplers can, in principle, only cancel couplings between NN qubits coupled via them, and have no mechanism to cancel the other couplings, $g_{13}$ is always active. It means that a larger $|g_{13}|$ will lead to more serious errors in the $Q_1$-$Q_3$ subspace, such as microwave crosstalk. In fact, these errors are more pronounced for the STC than for the DTC (see Appendix H).

The above difference in $g_{13}/(2\pi)$ (0.13 and 1.62 MHz for the DTC and the STC architecture, respectively) arises from the structure of the coupler and the coupling cancelation mechanism. Since the STCs utilize the relatively large direct capacitances between the NN qubits, $C_{12}$ and $C_{23}$, for canceling residual couplings [3], NN qubits tend to be close to each other. This makes NNN qubits close as well, and thus the capacitance between the NNN qubits $C_{13}$ tends to be large (0.03 fF). On the other hand, the DTC does not require $C_{12}$ and $C_{23}$, allowing for greater distances between NN qubits and hence between NNN qubits, leading to a smaller $C_{13}$ (0.003 fF). This difference in $C_{13}$ is a major reason for the difference in $g_{13}$.

Note that even if $C_{13}$ is zero, there is still an effective capacitance, and hence the $g_{13}$ is not zero: 0.04 and 0.71 MHz for the DTC and the STC architecture, respectively. The one in the STC still remains about a half of the original value.

In an ideal limit where all parasitic capacitances are zero, $g_{13}/(2\pi)$ of the DTC and STC become 0.00 and 0.38 MHz, respectively. This means that in the DTC architecture, $g_{13}$ arises through parasitic capacitances and vanishes in the ideal situation. On the other hand, even in this ideal situation, $g_{13}$ in the STC architecture is about a half of that before taking the limit.

The remaining $g_{13}$ in the STC architecture is determined by two factors. One of them is the direct couplings between NN qubits, namely $C_{12}$ and $C_{23}$. In the STC architecture, they are large for canceling residual couplings as mentioned above, and thus this contribution does not vanish even in the above ideal situation with no parasitic capacitances. On the other hand, the DTC does not rely on $C_{12}$ and $C_{13}$, that is, $C_{12}$ and $C_{23}$ are parasitic capacitances for the DTC architecture, and hence the contribution is negligible.

The other factor is the indirect couplings through a coupler transmon. This contribution can be estimated by considering the case where $C_{12}$ and $C_{23}$ are zero, resulting in 0.11 MHz for the STC architecture. In the DTC architecture, corresponding contribution is negligible because the coupling between the two transmons inside DTC $L(R)$ is nearly disconnected due to the small parasitic capacitance $C_{45}(C_{67})$.

In summary, the higher performance of the DTC architecture than the STC one mainly comes from the fact that the DTC has the advantage that it can reduce the NNN coupling, $g_{13}$, compared to the STC from various points.

## VI. SUMMARY

In this paper, we have analyzed the system of three fixed-frequency-transmon qubits coupled via two DTCs, by numerical simulation using the circuit model, where the NN qubits are highly detuned and NNN qubits are nearly resonant. As a result, we have found that the DTC can suppress the residual *ZZ* couplings and *ZZZ* coupling, as well as in isolated two-qubit systems. Moreover, we have succeeded in implementing 30-ns CZ gates and not only individual but also simultaneous 10-ns $\pi/2$ pulses with average fidelities over 99.99%. The degradation of the CZ gate fidelities due to the increasing number of qubits from two to three is negligible in the four-digit precision.

For comparison, additional simulations of the system where DTCs were replaced by STCs have been performed. Then, we have found that both suppressing residual couplings to several kHz and achieving two-qubit and single-qubit gates with fidelities of 99.99% are highly challenging for the STCs. Due to the structure of STCs, the NNN-qubit coupling strength $g_{13}$ tends to be larger than DTCs, and hence causes more severe errors.

From these results, we have concluded that the DTC architecture is more promising than the STC architecture

for realizing high-performance, scalable superconducting quantum computers. We expect that our results will be confirmed experimentally in the near future.

## APPENDIX A: DERIVATION OF THE HAMILTONIAN

### 1. DTC architecture

The Lagrangian $L$ describing the system in Fig. 2(a) is given as follows:

$$L = K - U, \tag{A1}$$

$$K = \sum_{i=1}^{7} \frac{C_{ii}}{2} \dot{\phi}_i^2 + \sum_{i=1}^{3} \sum_{j=i+1}^{7} \frac{C_{ij}}{2} (\dot{\phi}_i - \dot{\phi}_j)^2$$

$$+ \sum_{i=4}^{5} \sum_{j=6}^{7} \frac{C_{ij}}{2} (\dot{\phi}_i - \dot{\phi}_j)^2$$

$$+ \frac{C_{45}}{2} \dot{\phi}_8^2 + \frac{C_{67}}{2} \dot{\phi}_9^2 + \sum_{i=1}^{3} \frac{C_{di}}{2} (\dot{\phi}_i - V_i)^2, \tag{A2}$$

$$U = -\sum_{i=1}^{7} \hbar\omega_{J_i} \cos\varphi_i - \hbar\omega_{J8} \cos(\varphi_8) - \hbar\omega_{J9} \cos(\varphi_9). \tag{A3}$$

Using the constraints $\phi_8 = \phi_5 - \phi_4 - \Phi_{\text{ex},L}$ and $\phi_9 = \phi_7 - \phi_6 - \Phi_{\text{ex},R}$ and neglecting the constant terms, the $K$ and $U$ are rewritten as follows:

$$K = \frac{1}{2} \dot{\phi}^T M \dot{\phi} - \mathbf{q}_D^T \dot{\phi} - \frac{e}{4} \alpha^T \dot{\phi}, \tag{A4}$$

$$U = -\sum_{i=1}^{7} \hbar\omega_{J_i} \cos\varphi_i$$

$$- \hbar\omega_{J8} \cos(\varphi_5 - \varphi_4 - \Theta_{\text{ex},L})$$

$$- \hbar\omega_{J9} \cos(\varphi_7 - \varphi_6 - \Theta_{\text{ex},R}), \tag{A5}$$

where

$$\phi^T = (\phi_1, \phi_2, \phi_3, \phi_4, \phi_5, \phi_6, \phi_7), \tag{A6}$$

$$\mathbf{q}_D^T = (0, 0, 0, -C_{45}\dot{\Phi}_{\text{ex},L}, C_{45}\dot{\Phi}_{\text{ex},L}, -C_{67}\dot{\Phi}_{\text{ex},R}, C_{67}\dot{\Phi}_{\text{ex},R})$$

$$= \frac{e}{4} (\dot{\Theta}_{\text{ex},L} \mathbf{t}_{DL}^T + \dot{\Theta}_{\text{ex},R} \mathbf{t}_{DR}^T), \tag{A7}$$

$$\alpha^T = (\alpha_1, \alpha_2, \alpha_3, 0, 0, 0, 0), \tag{A8}$$

with $\alpha_i = 2eV_i/(\hbar\omega_{C_{di}})$ for $i \in \{1,2,3\}$ and $\mathbf{t}_{D\mu}^T$ for $\mu \in \{L, R\}$ defined by Eqs. (3) and (4).

The Hamiltonian is obtained by the Legendre transformation of $L$ as

$$H = \mathbf{Q}^T \dot{\phi} - L$$

$$= \frac{1}{2} \mathbf{Q}^T M^{-1} \mathbf{Q} + \mathbf{q}_D^T M^{-1} \mathbf{Q} + \frac{e}{4} \alpha^T M^{-1} \mathbf{Q} + U, \tag{A9}$$

$$\mathbf{Q} = \frac{\partial L}{\partial \dot{\phi}} = M\dot{\phi} - \mathbf{q}_D - \frac{e}{4} \alpha, \tag{A10}$$

where $\mathbf{Q}$ denotes charge variables that are canonical conjugate variables for the flux variables $\phi$. Introducing the Cooper-pair number variables as $\mathbf{n} = \mathbf{Q}/(2e)$, $H$ is rewritten as follows:

$$H = 4\hbar \mathbf{n}^T W \mathbf{n} + (\dot{\Theta}_{\text{ex},L} \mathbf{t}_{DL}^T + \dot{\Theta}_{\text{ex},R} \mathbf{t}_{DR}^T) \hbar W \mathbf{n}$$

$$+ \alpha^T \hbar W \mathbf{n} + U. \tag{A11}$$

By canonical quantization procedure, namely, replacing the classical values $\mathbf{n}$ and $\phi$, respectively, with operators $\hat{\mathbf{n}}$ and $\hat{\phi}$ satisfying the canonical commutation relation $[\hat{\varphi}_i, \hat{n}_j] = i\delta_{i,j}$, we obtain the quantized Hamiltonian:

$$\hat{H} = 4\hbar \hat{\mathbf{n}}^T W \hat{\mathbf{n}} + (\dot{\Theta}_{\text{ex},L} \mathbf{t}_{DL}^T + \dot{\Theta}_{\text{ex},R} \mathbf{t}_{DR}^T) \hbar W \hat{\mathbf{n}}$$

$$+ \alpha^T \hbar W \hat{\mathbf{n}} + \hat{U}. \tag{A12}$$

As special cases, Eq. (1) is obtained when $\boldsymbol{\alpha} = \mathbf{0}$ and Eq. (22) is obtained when $(\Theta_{\text{ex},L}, \Theta_{\text{ex},R}) = (\Theta_{\text{Id},L}, \Theta_{\text{Id},R})$, $\alpha_i \neq 0$, and $\alpha_j = 0$ for $j \neq i$. The Hamiltonian of the isolated two-qubit systems $\hat{H}^{L(R)}$ can also be derived in a similar manner.

### 2. STC architecture

The Lagrangian $L$ describing the system in Fig. 4(a) is given as follows:

$$L = K - U, \tag{A13}$$

$$K = \sum_{i=1}^{3} \frac{C_{ii}}{2} \dot{\phi}_i^2 + \sum_{i=4}^{5} \sum_{v \in \{A,B\}} \frac{C_{iiv}}{2} \dot{\phi}_{iv}^2$$

$$+ \sum_{i=1}^{2} \sum_{j=i+1}^{3} \frac{C_{ij}}{2} (\dot{\phi}_j - \dot{\phi}_i)^2$$

$$+ \sum_{i=1}^{3} \sum_{j=4}^{5} \sum_{v \in \{A,B\}} \frac{1}{2} \frac{C_{ij}}{2} (\dot{\phi}_{jv} - \dot{\phi}_i)^2$$

$$+ \sum_{v_1, v_2 \in \{A,B\}} \frac{1}{2} \frac{C_{45}}{4} (\dot{\phi}_{5v_1} - \dot{\phi}_{4v_2})^2 + \sum_{i=1}^{3} \frac{C_{di}}{2} (\dot{\phi}_i - V_i)^2, \tag{A14}$$

$$U = -\sum_{i=1}^{3} \hbar\omega_{Ji}\cos\varphi_i - \sum_{i=4}^{5}\sum_{v\in\{A,B\}}\hbar\omega_{Jiv}\cos\varphi_{iv}, \quad \text{(A15)}$$

Using the constraints $\phi_{4B} = \phi_{4A} - \Phi_{\mathrm{ex},L}$ and $\phi_{5B} = \phi_{5A} - \Phi_{\mathrm{ex},R}$, the addition theorem, and neglecting the constant terms, $K$ and $U$ are rewritten as follows:

$$K = \frac{1}{2}\dot{\phi}^T M\dot{\phi} - \mathbf{q}_S^T\dot{\phi} - \frac{e}{4}\alpha^T\dot{\phi}, \quad \text{(A16)}$$

$$\begin{aligned}
U = &-\sum_{i=1}^{3}\hbar\omega_{Ji}\cos(\varphi_i) \\
&- \left[\hbar\omega_{J4A} + \hbar\omega_{J4B}\cos(\Theta_{\mathrm{ex},L})\right]\cos(\varphi_4) \\
&- \hbar\omega_{J4B}\sin(\Theta_{\mathrm{ex},L})\sin(\varphi_4) \\
&- \left[\hbar\omega_{J5A} + \hbar\omega_{J5B}\cos(\Theta_{\mathrm{ex},R})\right]\cos(\varphi_5) \\
&- \hbar\omega_{J5B}\sin(\Theta_{\mathrm{ex},R})\sin(\varphi_5), \quad \text{(A17)}
\end{aligned}$$

where

$$\phi^T = (\phi_1, \phi_2, \phi_3, \phi_4, \phi_5), \quad \text{(A18)}$$

$$\mathbf{q}_S^T = \frac{e}{4}(\dot{\Theta}_{\mathrm{ex},L}\mathbf{t}_{SL}^T+, \dot{\Theta}_{\mathrm{ex},R}\mathbf{t}_{SR}^T), \quad \text{(A19)}$$

$$\alpha^T = (\alpha_1, \alpha_2, \alpha_3, 0, 0), \quad \text{(A20)}$$

with $\mathbf{t}_{S\mu}^T$ for $\mu \in \{L, R\}$ defined by Eqs. (25) and (26), and we have simply written $\phi_{4A(5A)}$ as $\phi_{4(5)}$. We can obtain the Hamiltonian by the Legendre transformation of $L$ as

$$\begin{aligned}
H = &4\hbar\mathbf{n}^T W\mathbf{n} + \left(\dot{\Theta}_{\mathrm{ex},L}\mathbf{t}_{SL}^T + \dot{\Theta}_{\mathrm{ex},R}\mathbf{t}_{SR}^T\right)\hbar W\mathbf{n} \\
&+ \alpha^T\hbar W\mathbf{n} + U. \quad \text{(A21)}
\end{aligned}$$

By canonical quantization of it, we obtain the following quantized Hamiltonian:

$$\begin{aligned}
\hat{H} = &4\hbar\hat{\mathbf{n}}^T W\hat{\mathbf{n}} + \left(\dot{\Theta}_{\mathrm{ex},L}\mathbf{t}_{SL}^T + \dot{\Theta}_{\mathrm{ex},R}\mathbf{t}_{SR}^T\right)\hbar W\hat{\mathbf{n}} \\
&+ \alpha^T\hbar W\hat{\mathbf{n}} + \hat{U}. \quad \text{(A22)}
\end{aligned}$$

Equation (23) is obtained when $\alpha = \mathbf{0}$. The Hamiltonian of the isolated two-qubit systems $\hat{H}^{L(R)}$ can also be derived in a similar manner.

## APPENDIX B: MATRIX REPRESENTATION OF THE HAMILTONIAN

The matrix representations of the operators $\hat{n}_i$, $\cos\hat{\varphi}_i$, and $\sin\hat{\varphi}_i$ in the basis of $\hat{n}_i$ eigenfunctions are given as

follows:

$$\hat{n}_i = \begin{pmatrix} -N & & \\ & \ddots & \\ & & N \end{pmatrix}, \quad \text{(B1)}$$

$$\cos\hat{\varphi}_i = \frac{1}{2}\begin{pmatrix} & 1 & & \\ 1 & & \ddots & \\ & \ddots & & 1 \\ & & 1 & \end{pmatrix}, \quad \text{(B2)}$$

$$\sin\hat{\varphi}_i = \frac{1}{2i}\begin{pmatrix} & -1 & & \\ 1 & & \ddots & \\ & \ddots & & -1 \\ & & 1 & \end{pmatrix}, \quad \text{(B3)}$$

where $N$ is a cutoff for the Cooper-pair number. Each operator is expressed as a $(2N+1) \times (2N+1)$ matrix.

Since the total system shown in Fig. 2(a) is composed of seven subsystems (transmons), each operator in Eq. (1) is replaced by a tensor product of seven operators, such as $\hat{n}_1 \otimes \hat{I}_2 \otimes \hat{I}_3 \otimes \hat{I}_4 \otimes \hat{I}_5 \otimes \hat{I}_6 \otimes \hat{I}_7$, where $\hat{I}_i$ is the identity operator for the $i$th subsystem of $\hat{\varphi}_i$ and $\hat{n}_i$. From the addition theorem, $\cos(\hat{\varphi}_5 - \hat{\varphi}_4 - \Theta_{\mathrm{ex},L})$ and $\cos(\hat{\varphi}_7 - \hat{\varphi}_6 - \Theta_{\mathrm{ex},R})$ are, respectively, expressed as follows:

$$\begin{aligned}
&\cos(\hat{\varphi}_5 - \hat{\varphi}_4 - \Theta_{\mathrm{ex},L}) \\
&= \hat{I}_1 \otimes \hat{I}_2 \otimes \hat{I}_3 \\
&\otimes \Big\{\cos\Theta_{\mathrm{ex},L}\left[\cos(\hat{\varphi}_4) \otimes \cos(\hat{\varphi}_5) + \sin(\hat{\varphi}_4) \otimes \sin(\hat{\varphi}_5)\right] \\
&+ \sin\Theta_{\mathrm{ex},L}\left[\cos(\hat{\varphi}_4) \otimes \sin(\hat{\varphi}_5) - \sin(\hat{\varphi}_4) \otimes \cos(\hat{\varphi}_5)\right]\Big\} \\
&\otimes \hat{I}_6 \otimes \hat{I}_7, \quad \text{(B4)}
\end{aligned}$$

$$\begin{aligned}
&\cos(\hat{\varphi}_7 - \hat{\varphi}_6 - \Theta_{\mathrm{ex},R}) \\
&= \hat{I}_1 \otimes \hat{I}_2 \otimes \hat{I}_3 \otimes \hat{I}_4 \otimes \hat{I}_5 \\
&\otimes \Big\{\cos\Theta_{\mathrm{ex},R}\left[\cos(\hat{\varphi}_6) \otimes \cos(\hat{\varphi}_7) + \sin(\hat{\varphi}_6) \otimes \sin(\hat{\varphi}_7)\right] \\
&+ \sin\Theta_{\mathrm{ex},R}\left[\cos(\hat{\varphi}_6) \otimes \sin(\hat{\varphi}_7) - \sin(\hat{\varphi}_6) \otimes \cos(\hat{\varphi}_7)\right]\Big\}. \\
&\quad \text{(B5)}
\end{aligned}$$

In the matrix representation, $\hat{I}_i$ is given by the $(2N+1) \times (2N+1)$ identity matrix and the tensor product $\otimes$ is replaced by the Kronecker product of matrices. Thus, we obtain a $(2N+1)^7 \times (2N+1)^7$ matrix representation of the Hamiltonian in Eq. (1).

Similarly, we can obtain a $(2N+1)^5 \times (2N+1)^5$ matrix representation of the Hamiltonian in Eq. (23).

## APPENDIX C: DIMENSION-REDUCTION TECHNIQUE

In this section, we introduce our numerical method to reduce the computational cost. Here we explain only the case of the three-qubit system with two DTCs. Other systems can also be treated similarly.

### 1. Diagonalization

The Hamiltonian in Eq. (1) can be divided as follows.

$$\hat{H} = \hat{H}_{123} + \hat{H}_{45} + \hat{H}_{67} + \hat{H}_{\text{int}}, \tag{C1}$$

$$\hat{H}_{123} = \sum_{i=1}^{3} \left( 4\hbar W_{ii}\hat{n}_i^2 - \hbar\omega_{J_i}\cos\hat{\varphi}_i \right), \tag{C2}$$

$$\hat{H}_{45} = \sum_{i=4}^{5} \left( 4\hbar W_{ii}\hat{n}_i^2 - \hbar\omega_{J_i}\cos\hat{\varphi}_i \right)$$
$$- \hbar\omega_{J_8}\cos(\hat{\varphi}_5 - \hat{\varphi}_4 - \Theta_{\text{ex},L}), \tag{C3}$$

$$\hat{H}_{67} = \sum_{i=6}^{7} \left( 4\hbar W_{ii}\hat{n}_i^2 - \hbar\omega_{J_i}\cos\hat{\varphi}_i \right)$$
$$- \hbar\omega_{J_9}\cos(\hat{\varphi}_7 - \hat{\varphi}_6 - \Theta_{\text{ex},R}), \tag{C4}$$

$$\hat{H}_{\text{int}} = \sum_{i=1}^{3}\sum_{j=4}^{7} 8\hbar W_{ij}\hat{n}_i\hat{n}_j + \sum_{i=4}^{5}\sum_{j=6}^{7} 8\hbar W_{ij}\hat{n}_i\hat{n}_j. \tag{C5}$$

Here, $\hat{H}_{123}$, $\hat{H}_{45}$, and $\hat{H}_{67}$ correspond to the qubit, DTC-$L$, and DTC-$R$ subspaces, respectively, and $\hat{H}_{\text{int}}$ is the interaction Hamiltonian between them.

The qubit-subspace Hamiltonian $\hat{H}_{123}$ is expressed by $(2N+1)^3 \times (2N+1)^3$ matrix. We diagonalize it using SciPy [49] to obtain the eigenenergy matrix $\hat{e}_{123}$ and the energy eigenstate matrix $\hat{V}_{123}$ satisfying the following relation:

$$\hat{V}_{123}^{\dagger}\hat{H}_{123}\hat{V}_{123} = \hat{e}_{123}, \tag{C6}$$

where the diagonal components of $\hat{e}_{123}$ are the eigenenergies of $\hat{H}_{123}$ in the ascending order. We introduce the cutoff $N_{123}$ to restrict the matrix size of $\hat{e}_{123}$ and $\hat{V}_{123}$ to $N_{123} \times N_{123}$. Using $\hat{V}_{123}$, we can obtain $\hat{n}_i'$ for $i \in \{1,2,3\}$, which is the $\hat{n}_i$ represented by the $\hat{V}_{123}$ basis as follows:

$$\hat{n}_i' = \hat{V}_{123}^{\dagger}\hat{n}_i\hat{V}_{123} \text{ for } i \in \{1,2,3\}. \tag{C7}$$

This procedure reduces the matrix size of $\hat{n}_i$ from $(2N+1)^3 \times (2N+1)^3$ to $N_{123} \times N_{123}$. In this work, we set $N_{123}$ to 120. Similarly, we reduce the matrix size of $\hat{n}_i$ for $i \in$ {4,5,6,7} as follows:

$$\hat{n}_i' = \hat{V}_{45}^{\dagger}\hat{n}_i\hat{V}_{45} \text{ for } i \in \{4,5\}, \tag{C8}$$

$$\hat{n}_i' = \hat{V}_{67}^{\dagger}\hat{n}_i\hat{V}_{67} \text{ for } i \in \{6,7\}, \tag{C9}$$

where the eigenstate matrices $\hat{V}_{45}$ and $\hat{V}_{67}$ satisfy the following equations:

$$\hat{V}_{45}^{\dagger}\hat{H}_{45}\hat{V}_{45} = \hat{e}_{45}, \tag{C10}$$

$$\hat{V}_{67}^{\dagger}\hat{H}_{67}\hat{V}_{67} = \hat{e}_{67}. \tag{C11}$$

The diagonal components of the eigenenergy matrices $\hat{e}_{45}$ and $\hat{e}_{67}$ are the eigenenergies of $\hat{H}_{45}$ and $\hat{H}_{67}$, respectively, in the ascending order. Here, we introduce the cutoff $N_{45}$ and $N_{56}$ to restrict the matrix size of $(\hat{e}_{45}, \hat{V}_{45})$ and $(\hat{e}_{67}, \hat{V}_{67})$ to $N_{45} \times N_{45}$ and $N_{67} \times N_{67}$, respectively. In this work, we set both $N_{45}$ and $N_{67}$ to 25.

Using them, we obtain the Hamiltonian with reduced matrix size as follows:

$$\hat{H}' = \hat{e}_{123} + \hat{e}_{45} + \hat{e}_{67} + \hat{H}_{\text{int}}', \tag{C12}$$

$$\hat{H}_{\text{int}}' = \sum_{i=1}^{3}\sum_{j=4}^{7} 8\hbar W_{ij}\hat{n}_i'\hat{n}_j' + \sum_{i=4}^{5}\sum_{j=6}^{7} 8\hbar W_{ij}\hat{n}_i'\hat{n}_j'. \tag{C13}$$

The size of these matrices is $(N_{123} \times N_{45} \times N_{67}) \times (N_{123} \times N_{45} \times N_{67}) = 75000 \times 75000$. By diagonalizing $\hat{H}'$, we can obtain the energy eigenvalues of the total system.

We have set the dimensions as $N_{123} = 120$ and $N_{45} = N_{67} = 25$ for sufficient convergence of eigenfrequencies with sub-kHz accuracy. By this method, the matrix size of the Hamiltonian for diagonalizations is greatly reduced from $(2N+1)^7 \times (2N+1)^7 = 1801088541 \times 1801088541$ to $(N_{123} \times N_{45} \times N_{67}) \times (N_{123} \times N_{45} \times N_{67}) = 75000 \times 75000$.

### 2. Gate simulation

We explain the gate simulation method. As an example, we consider the case of the CZ gate for $Q_1$ and $Q_2$.

From the results of the diagonalization of the total Hamiltonian explained in the previous subsection, we identify the idle point. Fixing $\Theta_{\text{ex},R}$ to $\Theta_{\text{Id},R}$, we again diagonalize $\hat{H}'$ for $\Theta_{\text{ex},L} = \Theta_n = 0.05n\pi$ ($n = 0, 1, \ldots, 20$) to obtain the eigenenergy matrix $\hat{e}_0(\Theta_n)$ and the energy eigenstate matrix $\hat{V}_0(\Theta_n)$ satisfying the following relation:

$$\hat{V}_0(\Theta_n)^{\dagger}\hat{H}'(\Theta_n)\hat{V}_0(\Theta_n) = \hat{e}_0(\Theta_n), \tag{C14}$$

where the diagonal components of $\hat{e}_0(\Theta_n)$ are the eigenenergies of $\hat{H}'(\Theta_n)$ in the ascending order. We introduce the cutoff $N_0$ to restrict the matrix size of $\hat{e}_0(\Theta_n)$ and $\hat{V}_0(\Theta_n)$

to $N_0 \times N_0$. In this work, we set $N_0$ to 1000. Using $\hat{V}_0(\Theta_n)$, we calculate the following matrices:

$$\hat{P}(\Theta_n) = \left[ \hat{V}_{123} \otimes \hat{V}_{45}(\Theta_n) \otimes \hat{V}_{67} \right] \hat{V}_0(\Theta_n), \qquad \text{(C15)}$$

and express the Hamiltonian at the magnetic flux $\Theta_{\text{ex},L} \in \mathscr{R}_m = [\Theta_m - 0.025\pi, \Theta_m + 0.025\pi)$ as

$$\begin{aligned} \hat{H}''(\Theta_{\text{ex},L}) = &\; \hat{e}_0(\Theta_m) \\ &+ \dot{\Theta}_{\text{ex},L} \mathbf{t}_{DL}^T \hat{P}^\dagger(\Theta_m) \hbar W \hat{\mathbf{n}} \hat{P}(\Theta_m) \\ &- \hbar \omega_{J_8} \hat{P}^\dagger(\Theta_m) \hat{c}(\Theta_{\text{ex},L}) \hat{P}(\Theta_m), \qquad \text{(C16)} \end{aligned}$$

$$\begin{aligned} \hat{c}(\Theta_{\text{ex},L}) = &\; \cos(\hat{\varphi}_5 - \hat{\varphi}_4 - \Theta_{\text{ex},L}) \\ &- \cos(\hat{\varphi}_5 - \hat{\varphi}_4 - \Theta_m). \qquad \text{(C17)} \end{aligned}$$

The matrix size of $\hat{H}''$ is $N_0 \times N_0 = 1000 \times 1000$. When $\Theta_{\text{ex},L}(t) \in \mathscr{R}_m$, we calculate the time evolution of the state vector represented by the $\hat{P}_0(\Theta_m)$ basis, using the above Hamiltonian $\hat{H}''$ and QuTiP [47,48]. At the particular time when the range including $\Theta_{\text{ex},L}$ changes from $\mathscr{R}_m$ to $\mathscr{R}_{m+1}$ or to $\mathscr{R}_{m-1}$, we operate the following basis transformation matrices:

$$\hat{P}_{\text{inc}}(\Theta_m) = \hat{P}(\Theta_{m+1}) \hat{P}^\dagger(\Theta_m), \qquad \text{(C18)}$$

$$\hat{P}_{\text{dec}}(\Theta_m) = \hat{P}(\Theta_{m-1}) \hat{P}^\dagger(\Theta_m), \qquad \text{(C19)}$$

respectively, on the state vector.

We have set the dimensions as $N_{123} = 120$, $N_{45} = N_{67} = 25$, and $N_0 = 1000$ for sufficient convergence of average fidelities with accuracy of the order of $10^{-5}$. By this method, the matrix size of the Hamiltonian for gate simulations is greatly reduced from $(2N + 1)^7 \times (2N + 1)^7 = 1801088541 \times 1801088541$ to $N_0 \times N_0 = 1000 \times 1000$.

## APPENDIX D: ISOLATED TWO-QUBIT SUBSYSTEMS *L* AND *R*

### 1. DTC architecture

The Hamiltonian of the system $\mu \in \{L, R\}$ is denoted by $\hat{H}^\mu$ (see Appendix A and Ref. [29] for help of the derivation). Its eigenfrequencies and corresponding eigenstates are denoted by $\omega_{Q_1,Q_2,C_4,C_5}^L$ $\left( \omega_{Q_2,Q_3,C_6,C_7}^R \right)$ and $|Q_1, Q_2, C_4, C_5\rangle_L$ $\left( |Q_2, Q_3, C_6, C_7\rangle_R \right)$, respectively. We also use notations $\omega_{Q_1,Q_2}^L \equiv \omega_{Q_1,Q_2,0,0}^L$ $\left( \omega_{Q_2,Q_3}^R \equiv \omega_{Q_2,Q_3,0,0}^R \right)$ and $|Q_1, Q_2\rangle_L \equiv |Q_1, Q_2, 0, 0\rangle_L$ $\left( |Q_2, Q_3\rangle_R \equiv |Q_2, Q_3, 0, 0\rangle_R \right)$. Eigenfrequencies of the computational states in the system $L(R)$, $\omega_{0,0}^{L(R)}, \omega_{1,0}^{L(R)}, \omega_{0,1}^{L(R)}, \omega_{1,1}^{L(R)}$, as functions of

$\Theta_{\text{ex},L(R)}$ are shown by scatter plots in Figs. 3(a) and 3(b) where we have set $\omega_{0,0}^{L(R)}$ to 0 (outside the graph scale).

The *ZZ* couplings, $\zeta_{12}$ in the system *L* and $\zeta_{23}$ in the system *R* are calculated as follows:

$$\zeta_{12} = \omega_{1,1}^L - \omega_{1,0}^L - \omega_{0,1}^L + \omega_{0,0}^L, \qquad \text{(D1)}$$

$$\zeta_{23} = \omega_{1,1}^R - \omega_{1,0}^R - \omega_{0,1}^R + \omega_{0,0}^R. \qquad \text{(D2)}$$

These values should be as small as possible at the idle point to suppress conditional phase rotation which causes quantum crosstalk. As shown in Figs. 3(c) and 3(d) by the scatter plot, the minimum value of $|\zeta_{12(23)}|/(2\pi)$ is about 2(2) kHz at $\Theta_{\text{ex},L(R)} = 0.65\pi(0.65\pi) \equiv \Theta_{\text{Id},L(R)}$. Hence, we can choose $\Theta_{\text{Id},L}$ and $\Theta_{\text{Id},R}$ as idle points of system *L* and *R*, respectively.

### 2. STC architecture

Similarly to the DTC architecture, we define $\hat{H}^{L(R)}$. Its eigenfrequencies and corresponding eigenstates are denoted by $\omega_{Q_1,Q_2,C_4}^L$ $\left( \omega_{Q_2,Q_3,C_5}^R \right)$ and $|Q_1, Q_2, C_4\rangle_L$ $\left( |Q_2, Q_3, C_5\rangle_R \right)$, respectively. We also use notations $\omega_{Q_1,Q_2}^L \equiv \omega_{Q_1,Q_2,0}^L$ $\left( \omega_{Q_2,Q_3}^R \equiv \omega_{Q_2,Q_3,0}^R \right)$ and $|Q_1, Q_2\rangle_L \equiv |Q_1, Q_2, 0\rangle_L$ $\left( |Q_2, Q_3\rangle_R \equiv |Q_2, Q_3, 0\rangle_R \right)$. Eigenfrequencies of the computational states in the system $L(R)$, $\omega_{0,0}^{L(R)}, \omega_{1,0}^{L(R)}, \omega_{0,1}^{L(R)}, \omega_{1,1}^{L(R)}$, as functions of $\Theta_{\text{ex},L(R)}$ are shown by scatter plots in Figs. 6(a) and 6(b) where we have set $\omega_{0,0}^{L(R)}$ to 0 (outside the graph scale).

The *ZZ* couplings, $\zeta_{12}$ in the system *L* and $\zeta_{23}$ in the system *R* are calculated by Eqs. (D1) and (D2), respectively. As shown in Figs. 6(c) and 6(d) by the scatter plot, the minimum value of $|\zeta_{12(23)}|/(2\pi)$ is about 64(64) kHz at $\Theta_{\text{ex},L(R)} = 0(0) \equiv \Theta_{\text{Id},L(R)}$. Hence, we choose $\Theta_{\text{Id},L}$ and $\Theta_{\text{Id},R}$ as idle points of system *L* and *R*, respectively. The residual couplings are summarized in Table V. They are in good agreement with the result of Ref. [20]: about $-60$ kHz. Their magnitudes are roughly 30 times larger than the ones of the corresponding subsystems with the DTC.

## APPENDIX E: DEFINITION OF $\hat{U}'$

Here we explain the derivation of $\hat{U}'$ in Eq. (11) for average fidelity.

### 1. Three-qubit system

Using $|\widetilde{Q_1', Q_2', Q_3'}\rangle$, which is the resultant state of a gate operation on $|Q_1', Q_2', Q_3'\rangle$ ($Q_1', Q_2', Q_3' \in \{0, 1\}$), we define

$\hat{u}'$ as follows:

$$u'_{4Q_1+2Q_2+Q_3,4Q'_1+2Q'_2+Q'_3}$$
$$= \frac{\left(\langle 0,0,0|\widetilde{0,0,0}\rangle\right)^*}{\left|\langle 0,0,0|\widetilde{0,0,0}\rangle\right|} \langle Q_1,Q_2,Q_3|\widetilde{Q'_1,Q'_2,Q'_3}\rangle, \quad (E1)$$

where we have chosen the overall phase factor, $\left(\langle 0,0,0|\widetilde{0,0,0}\rangle\right)^*/\left|\langle 0,0,0|\widetilde{0,0,0}\rangle\right|$, such that $u'_{0,0}$ is equal to $|u'_{0,0}|$. Moreover, to account for the local single-qubit phase, we define $\hat{U}'$ as

$$\hat{U}' = \hat{P}_Z(\psi_1,\psi_2,\psi_3)\hat{u}'\hat{P}_Z^\dagger(\psi'_1,\psi'_2,\psi'_3), \quad (E2)$$

$$\hat{P}_Z(\psi_1,\psi_2,\psi_3) =$$
$$\begin{pmatrix} 1 & 0 \\ 0 & e^{-i\psi_1} \end{pmatrix} \otimes \begin{pmatrix} 1 & 0 \\ 0 & e^{-i\psi_2} \end{pmatrix} \otimes \begin{pmatrix} 1 & 0 \\ 0 & e^{-i\psi_3} \end{pmatrix}. \quad (E3)$$

Phase rotation angles $\psi_i$ and $\psi'_i$ should be chosen appropriately for each ideal gate operation $\hat{U}_{\text{id}}$ (see Appendix F).

### 2. Two-qubit systems

Similarly to Eq. (E1), we define $\hat{u}'$ as follows:

$$u'_{2Q_1+Q_2,2Q'_1+Q'_2}$$
$$= \frac{\left(_{L(R)}\langle 0,0|\widetilde{0,0}\rangle_{L(R)}\right)^*}{\left|_{L(R)}\langle 0,0|\widetilde{0,0}\rangle_{L(R)}\right|}{}_{L(R)}\langle Q_1,Q_2|\widetilde{Q'_1,Q'_2}\rangle_{L(R)}. \quad (E4)$$

Moreover, to account for the local single-qubit phase, we define $\hat{U}'$ as follows:

$$\hat{U}' = \hat{P}_Z(\psi_1,\psi_2)\hat{u}'\hat{P}_Z^\dagger(\psi'_1,\psi'_2), \quad (E5)$$

$$\hat{P}_Z(\psi_1,\psi_2) = \begin{pmatrix} 1 & 0 \\ 0 & e^{-i\psi_1} \end{pmatrix} \otimes \begin{pmatrix} 1 & 0 \\ 0 & e^{-i\psi_2} \end{pmatrix}. \quad (E6)$$

Phase rotation angles $\psi_i$ and $\psi'_i$ should be chosen appropriately for each ideal gate operation $\hat{U}_{\text{id}}$ (see Appendix F).

## APPENDIX F: PHASE CALIBRATION

### 1. cz gate

As an example, we consider a CZ gate for $(Q_1,Q_2)$. In this case, we define the above angles as

$$\psi_1 = \arg(u'_{44}), \quad (F1)$$

$$\psi_2 = \arg(u'_{22}), \quad (F2)$$

$$\psi_3 = \arg(u'_{11}), \quad (F3)$$

$$\psi'_1 = \psi'_2 = \psi'_3 = 0. \quad (F4)$$

This is because when leakage errors, undesired transition, and undesired conditional phase rotation do not exist, the matrix form of $\hat{u}'$ can be written as follows:

$$\hat{u}' = \begin{pmatrix} 1 & & & \\ & e^{i\phi_{010}} & & \\ & & e^{i\phi_{100}} & \\ & & & -e^{i(\phi_{010}+\phi_{100})} \end{pmatrix} \otimes \begin{pmatrix} 1 & 0 \\ 0 & e^{i\phi_{001}} \end{pmatrix}$$
$$= \hat{P}_Z^\dagger(\phi_{100},\phi_{010},\phi_{001})\hat{U}_{\text{CZ},12}, \quad (F5)$$

where $\phi_{100} = \arg(u'_{44}), \phi_{010} = \arg(u'_{22})$, and $\phi_{001} = \arg(u'_{11})$. Similar calibrations are valid for the CZ gate for $(Q_2,Q_3)$ and the ones in the two-qubit subsystems.

### 2. $\pi/2$ pulse

Next, as an example, we consider a $\pi/2$ pulse for $Q_1$. In this case, we define the angles as

$$\psi_1 = \arg(u'_{44}) - \arg(-u'_{04}), \quad (F6)$$

$$\psi_2 = \arg(u'_{22}), \quad (F7)$$

$$\psi_3 = \arg(u'_{11}), \quad (F8)$$

$$\psi'_1 = -\arg(iu'_{04}), \quad (F9)$$

$$\psi'_2 = \psi'_3 = 0. \quad (F10)$$

This is because when leakage errors, undesired transition, and undesired conditional phase rotation do not exist, the matrix form of $\hat{u}'$ can be written as follows:

$$\hat{u}' = \frac{1}{\sqrt{2}}\begin{pmatrix} 1 & -ie^{i\phi_A} \\ -ie^{i(\phi_{100}-\phi_A)} & e^{i\phi_{100}} \end{pmatrix} \otimes \begin{pmatrix} 1 & 0 \\ 0 & e^{i\phi_{010}} \end{pmatrix}$$
$$\otimes \begin{pmatrix} 1 & 0 \\ 0 & e^{i\phi_{001}} \end{pmatrix}$$
$$= \hat{P}_Z^\dagger(\phi_{100}-\phi_A,\phi_{010},\phi_{001})\hat{U}_{\pi/2,\{1\}}\hat{P}_Z(-\phi_A,0,0), \quad (F11)$$

where $\phi_A = \arg(iu'_{04})$. Similar calibrations are valid for the $\pi/2$ pulses for $Q_2$ and $Q_3$.

## APPENDIX G: PULSE OPTIMIZATION

### 1. cz gate

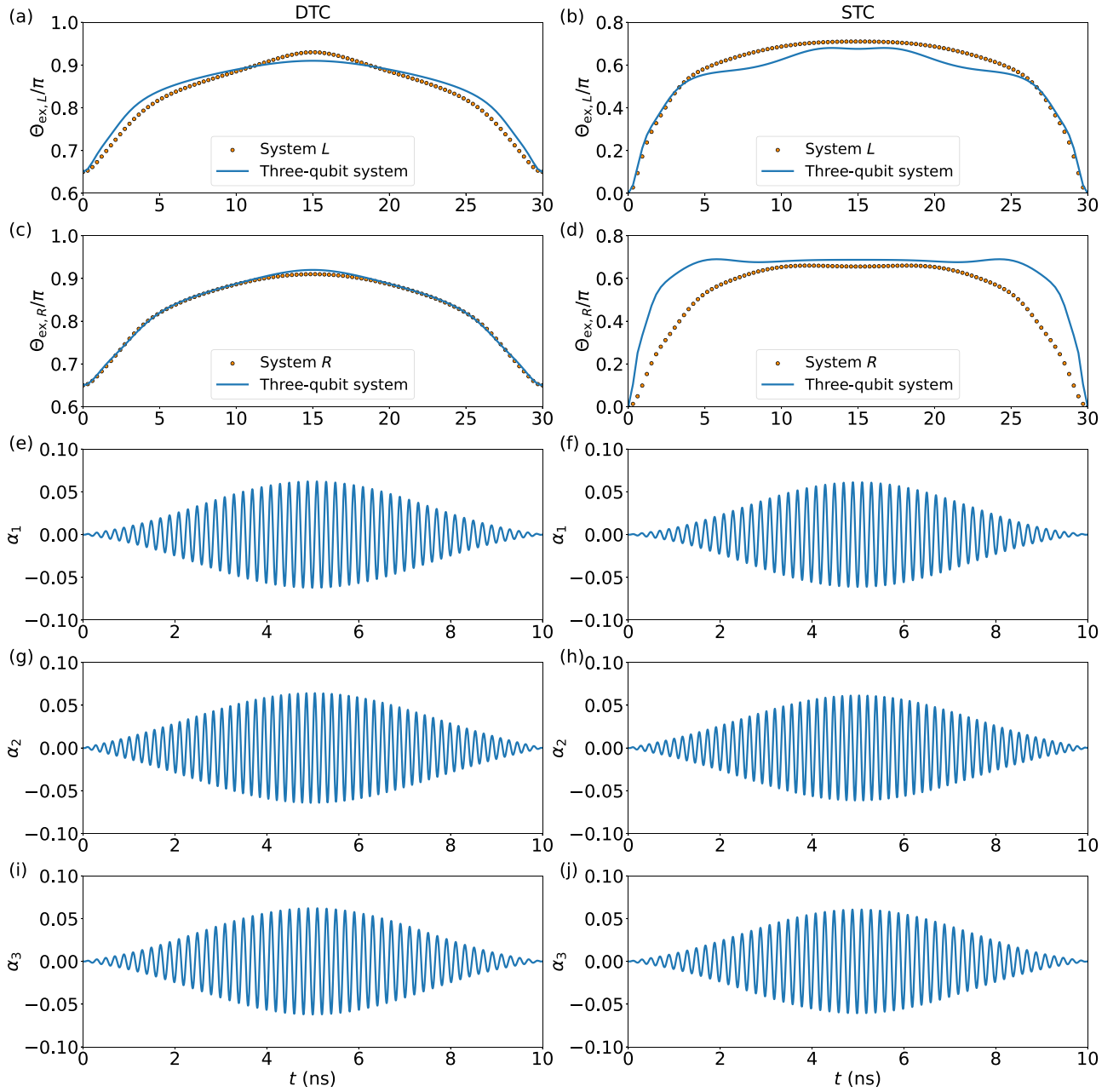We design the dc flux pulses for implementing CZ gates by the known technique to suppress leakage errors

FIG. 7. Optimized gate pulses. The left and right column correspond to the DTC and STC architectures, respectively. (a),(b) Optimized $\Theta_{\mathrm{ex},L}(t)$. (c),(d) Optimized $\Theta_{\mathrm{ex},R}(t)$. In (a)–(d), solid curves and scatter plots represent the pulses in three-qubit systems and two-qubit subsystems, respectively. (e),(f) Optimized $\alpha_1(t)$. (g),(h) Optimized $\alpha_2(t)$. (i),(j) Optimized $\alpha_3(t)$.

[29,30,50]. In the third-order design, $\Theta_{\mathrm{ex},\mu}(t)$ has the following form:

$$\theta_{L(R)}(t) = f_{L(R)}[\Theta_{\mathrm{Id},L(R)}]$$
$$+ \frac{f_{L(R)}[\Theta_{\mathrm{ex},L(R)}(t)] - f_{L(R)}[\Theta_{\mathrm{Id},L(R)}]}{2}$$
$$\times \sum_{n=1}^{3} \lambda_n \left(1 - \cos \frac{2n\pi t}{T}\right), \quad \text{(G1)}$$

where the hyperparameter $\lambda_n$ satisfies $\lambda_1 + \lambda_3 = 1$ and $f_{L(R)}$ is a numerical function of $\Theta_{\mathrm{ex},L(R)}$, which can be determined from an additional hyperparameter $\Theta_{P,L(R)}$ corresponding to a pulse peak and the spectrum data [Figs. 3(a) and 3(b) and Figs. 6(a) and 6(b) for the system with DTCs and STCs, respectively] (see Ref. [50] and Appendix C of Ref. [29] for the details). Applying the above $\Theta_{\mathrm{ex},L(R)}(t)$, we calculate infidelity $1 - \bar{F}_{\mathrm{CZ},12(23)}$ as a cost function, and optimize $\lambda_n$ by using the python version of the $L$-BFGS-$B$ optimizer of the optimparallel package [51,52]. We

iterate this optimization for different $\Theta_{P,L(R)} \in [\Theta_{\mathrm{Id},L(R)}, \pi]$ in increments of $0.01\pi$. We obtain the optimal pulse as the one with the lowest infidelity [see Figs. 7(a)–7(d) for their shapes].

### 2. $\pi/2$ pulse

It is known that applying a nonzero $\alpha_i$ modulated at the qubit frequency $\omega_{\mathrm{Id},i}$ of $Q_i$ at the idle point induces a Rabi oscillation in the $Q_i$ subspace. To suppress the nonadiabatic error, we assume the following DRAG-like pulse shape [53]:

$$\alpha_i = A_i(t)\sin(\omega_{\mathrm{Id},i}t) + B_i(t)\cos(\omega_{\mathrm{Id},i}t), \quad \text{(G2)}$$

$$A_i = a_i \frac{1}{2}\left(1 - \cos\frac{2\pi t}{T}\right), \quad \text{(G3)}$$

$$B_i = b_i \frac{\pi}{T}\frac{1}{\eta_i}\sin\frac{2\pi t}{T}, \quad \text{(G4)}$$

where $\eta_i$ is the anharmonicity of $Q_i$ at the idle point, and $T$ is the gate time. The values $a_i$ and $b_i$ are hyperparameters that determine the pulse shape. Applying the above $\alpha_i$, we calculate infidelity $1 - \bar{F}_{\pi/2,\{i\}}$ as a cost function, and optimize $a_i$ and $b_i$ by using python version of the *L*-BFGS-*B* optimizer of the optimparallel package [51,52]. We obtain the optimal pulse as the one with the lowest infidelity [see Figs. 7(e)–7(j) for their shapes].

### APPENDIX H: ERROR ANALYSIS

In this sections, we demonstrate that the STC architecture exhibits more pronounced errors in the $Q_1$-$Q_3$ subspace compared to the DTC architecture.

### 1. Microwave crosstalk during single-qubit gate operation

We first examine typical microwave crosstalk: undesired Rabi oscillation in the $Q_i$ subspace by the microwave pulse $\alpha_j$ ($i \neq j$). We denote its rotation angle as $\theta_{ji}$ and evaluate it from $\hat{U}'$ implemented by optimized microwave pulses $\alpha_j$.

We find that, in the DTC architecture, $|\theta_{13}| \sim |\theta_{31}| \sim 10^{-3}\pi$ and the other rotation angles are equal to or smaller than $10^{-5}\pi$. They are small enough to implement $\pi/2$ pulses with a fidelity over 99.99%.

On the other hand, in the STC architecture, while the most $|\theta_{ij}|$ are the same order as the DTC, only $|\theta_{13}|$ and $|\theta_{31}|$ are roughly 10 times larger. This may be caused by a relatively large $g_{13}$ of the STC architecture, as discussed in Sec. V. These results imply that the DTCs are more robust against microwave crosstalk than the STCs.
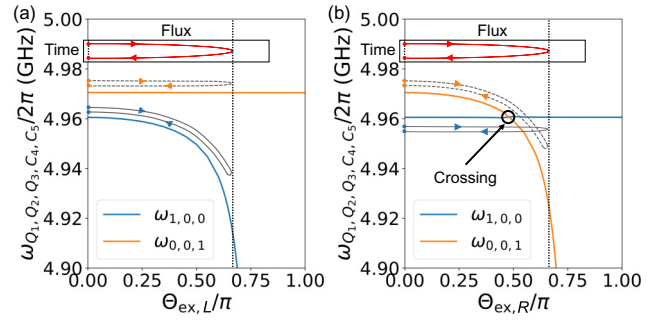


FIG. 8. Qubit frequencies during the CZ gate. (a),(b) show qubit frequencies, $\omega_{1,0,0}$ and $\omega_{0,0,1}$, as functions of $\Theta_{\mathrm{ex},L}$ and $\Theta_{\mathrm{ex},R}$, respectively. The inset figures show typical flux-pulse shapes [$\Theta_{\mathrm{ex},L}(t)$ and $\Theta_{\mathrm{ex},R}(t)$] for implementing CZ gates. The vertical dotted lines indicate the pulse peaks. The gray-solid lines and gray-dashed ones with arrows indicate trajectories of $\omega_{1,0,0}$ and $\omega_{0,0,1}$, respectively. Their trajectories are crossed only in (b). Note that $\Theta_{\mathrm{ex},R}$ in (a) and $\Theta_{\mathrm{ex},L}$ in (b) are fixed to the idle points.

### 2. Transition between $|1,Q_2,0\rangle$ and $|0,Q_2,1\rangle$ during CZ-gate operation

Next, we examine the errors during the CZ-gate operation from $\hat{U}'$ implemented by the flux pulse $\Theta_{\mathrm{ex},L(R)}$.

As a result, we find that all the off-diagonal elements of $\hat{U}'$ have an absolute value smaller than $10^{-2}$ in the DTC architecture. In other words, undesired transitions are almost negligible during a CZ gate in the DTC architecture, leading to the average gate fidelity over 99.99%.

On the other hand, in the STC architecture, the off-diagonal elements of $\hat{U}'$ corresponding to $\langle 1,Q_2,0|\widetilde{0,Q_2,1}\rangle$ and $\langle 0,Q_2,1|\widetilde{1,Q_2,0}\rangle$ are larger than $10^{-2}$. This result indicates that the SWAP-like transitions in the $Q_1$-$Q_3$ subspace occur during a CZ-gate operation. This leads to the gate-fidelity degradation. Furthermore, we found that the off-diagonal elements becomes larger for a CZ-gate operation on $(Q_2,Q_3)$ than on $(Q_1,Q_2)$. This can be explained by the crossing point of $\omega_{1,Q_2,0}$ and $\omega_{0,Q_2,1}$ during a CZ-gate operation on $(Q_2,Q_3)$, as shown in Fig. 8. The transitions corresponding to the off-diagonal elements lead to the result $\bar{F}_{\mathrm{CZ},23} < \bar{F}_{\mathrm{CZ},12}$ in Table V. These serious transitions also may be caused by a large $g_{13}$ discussed in Sec. V.

### APPENDIX I: DIAGONAL SETTING

In the main text, we considered the three-qubit systems in which the NNN qubits are located on the horizontal line like Fig. 1(a). To scale up a superconducting quantum computer, the diagonal structure such as the highlighted part of Fig. 9(a) is also relevant. Since the distances $Q_1$-$Q_3$, $Q_{1(3)}$-DTC $R(L)$, and DTC *L*-DTC *R* in this structure tend to be closer than the ones of the horizontal structure, the parasitic capacitances between them tend to increase.
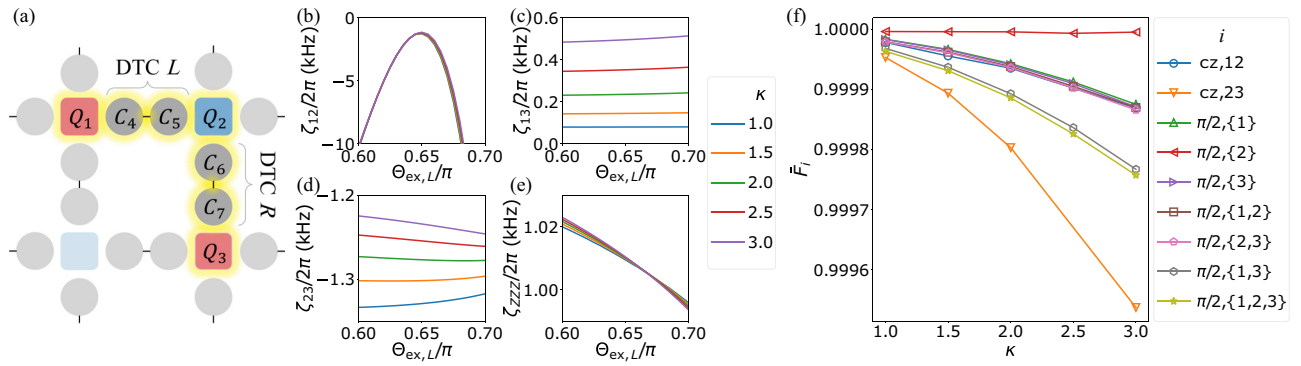
FIG. 9. (a) A three-qubit system of diagonal structure (highlighted part). (b)–(e) *ZZ* and *ZZZ* couplings around the idle point as functions of $\Theta_{\text{ex},L}$. Here, $\Theta_{\text{ex},R}$ is fixed to $\Theta_{\text{Id},R}$. (f) The average gate fidelities of 30-ns CZ gates and 10-ns $\pi/2$ pulses, implemented by optimized pulses, as functions of $\kappa$.

Therefore, it is necessary to clarify how the performance of the three-qubit system changes in response to the increases of the parasitic capacitances. Here, we investigate the case where the above parasitic capacitances, $C_{ij} = C_{ji}$ for $ij \in \{13, 16, 17, 34, 35, 46, 47, 56, 57\}$, are increased by a factor of $\kappa \in [1.0, 3.0]$ as follows:

$$C_{ij\,(ji)} \to \kappa C_{ij\,(ji)}. \quad (I1)$$

Figures 9(b)–9(e) show the *ZZ* and *ZZZ* couplings around the idle point. We find that the residual couplings do not increase by more than 1 kHz up to $\kappa = 3$. It means that the ability of the residual coupling suppression of the DTC is highly robust against the increase of the parasitic capacitances.

Figure 9(f) shows the average gate fidelities of 30-ns CZ gates and 10-ns $\pi/2$ pulses, implemented by optimized pulses, as functions of $\kappa$. The fidelities tend to decrease as $\kappa$ increases, in particular, for $\bar{F}_{\text{CZ},23}$, $\bar{F}_{\pi/2,\{1,3\}}$, and $\bar{F}_{\pi/2,\{1,2,3\}}$. This may be due to the effect of the crossing point and microwave crosstalk discussed in Appendix H. However, when $\kappa \lesssim 1.5$, all the gates can be implemented with fidelities of 99.99% or higher in the four-digit precision. Such parasitic capacitances may be experimentally feasible. Therefore, from these results, we expect that the DTC architecture can be extended to multiqubit systems while keeping its high performance.

[1] F. Arute, K. Arya, R. Babbush, D. Bacon, J. C. Bardin, R. Barends, R. Biswas, S. Boixo, F. G. Brandao, D. A. Buell *et al.*, Quantum supremacy using a programmable superconducting processor, Nature **574**, 505 (2019).
[2] Y. Wu *et al.*, Strong quantum computational advantage using a superconducting quantum processor, Phys. Rev. Lett. **127**, 180501 (2021).
[3] F. Yan, P. Krantz, Y. Sung, M. Kjaergaard, D. L. Campbell, T. P. Orlando, S. Gustavsson, and W. D. Oliver, Tunable coupling scheme for implementing high-fidelity two-qubit gates, Phys. Rev. Appl. **10**, 054062 (2018).
[4] I. Moskalenko, I. Besedin, I. Simakov, and A. Ustinov, Tunable coupling scheme for implementing two-qubit gates on fluxonium qubits, Appl. Phys. Lett. **119**, 194001 (2021).
[5] I. N. Moskalenko, I. A. Simakov, N. N. Abramov, A. A. Grigorev, D. O. Moskalev, A. A. Pishchimova, N. S. Smirnov, E. V. Zikiy, I. A. Rodionov, and I. S. Besedin, High fidelity two-qubit gates on fluxoniums using a tunable coupler, npj Quantum Inf. **8**, 130 (2022).
[6] L. Ding, M. Hays, Y. Sung, B. Kannan, J. An, A. DiPaolo, A. H. Karamlou, T. M. Hazard, K. Azar, D. K. Kim, B. M. Niedzielski, A. Melville, M. E. Schwartz, J. L. Yoder, T. P. Orlando, S. Gustavsson, J. A. Grover, K. Serniak, and W. D. Oliver, High-fidelity, frequency-flexible two-qubit fluxonium gates with a transmon coupler, Phys. Rev. X **13**, 031035 (2023).
[7] A. Petrescu, C. L. Calonnec, C. Leroux, A. D. Paolo, P. Mundada, S. Sussman, A. Vrajitoarea, A. A. Houck, and A. Blais, Accurate methods for the analysis of strong-drive effects in parametric gates, Phys. Rev. Appl. **19**, 044003 (2023).
[8] L. Jin, Implementing high-fidelity two-qubit gates in superconducting coupler architecture with novel parameter regions, arXiv:2105.13306.
[9] L. Heunisch, C. Eichler, and M. J. Hartmann, Tunable coupler to fully decouple and maximally localize superconducting qubits, Phys. Rev. Appl. **20**, 064037 (2023).
[10] E. A. Sete, A. Q. Chen, R. Manenti, S. Kulshreshtha, and S. Poletto, Floating tunable coupler for scalable quantum computing architectures, Phys. Rev. Appl. **15**, 064063 (2021).
[11] F. Marxer *et al.*, Long-distance transmon coupler with CZ-gate fidelity above 99.8%, PRX Quantum **4**, 010314 (2023).
[12] H. Wang, Y.-J. Zhao, H.-C. Sun, X.-W. Xu, Y. Li, Y. Zheng, Q. Liu, and R. Li, Controlling the qubit-qubit coupling in the superconducting circuit with double-resonator couplers, Phys. Rev. A **109**, 012601 (2024).
[13] Y. Chen *et al.*, Qubit architecture with high coherence and fast tunable coupling, Phys. Rev. Lett. **113**, 220502 (2014).
[14] C. Neill *et al.*, A blueprint for demonstrating quantum supremacy with superconducting qubits, Science **360**, 195 (2018).

[15] A. O. Niskanen, Y. Nakamura, and J.-S. Tsai, Tunable coupling scheme for flux qubits at the optimal point, Phys. Rev. B **73,** 094506 (2006).

[16] A. O. Niskanen, K. Harrabi, F. Yoshihara, Y. Nakamura, S. Lloyd, and J.-S. Tsai, Quantum coherent tunable coupling of superconducting qubits, Science **316,** 723 (2007).

[17] Y. Sung, L. Ding, J. Braumüller, A. Vepsäläinen, B. Kannan, M. Kjaergaard, A. Greene, G. O. Samach, C. McNally, D. Kim, A. Melville, B. M. Niedzielski, M. E. Schwartz, J. L. Yoder, T. P. Orlando, S. Gustavsson, and W. D. Oliver, Realization of high-fidelity CZ and ZZ-free iSWAP gates with a tunable coupler, Phys. Rev. X **11,** 021058 (2021).

[18] E. A. Sete, N. Didier, A. Q. Chen, S. Kulshreshtha, R. Manenti, and S. Poletto, Parametric-resonance entangling gates with a tunable coupler, Phys. Rev. Appl. **16,** 024050 (2021).

[19] Y. Xu, J. Chu, J. Yuan, J. Qiu, Y. Zhou, L. Zhang, X. Tan, Y. Yu, S. Liu, J. Li, F. Yan, and D. Yu, High-fidelity, high scalability two-qubit gate scheme for superconducting qubits, Phys. Rev. Lett. **125,** 240503 (2020).

[20] M. C. Collodo, J. Herrmann, N. Lacroix, C. K. Andersen, A. Remm, S. Lazar, J. Besse, T. Walter, A. Wallraff, and C. Eichler, Implementation of conditional phase gates based on tunable ZZ interactions, Phys. Rev. Lett. **125,** 240502 (2020).

[21] J. Stehlik, D. M. Zajac, D. L. Underwood, T. Phung, J. Blair, S. Carnevale, D. Klaus, G. A. Keefe, A. Carniol, M. Kumph, M. Steffen, and O. E. Dial, Tunable coupling architecture for fixed-frequency transmon superconducting qubits, Phys. Rev. Lett. **127,** 080505 (2021).

[22] J. Chu and F. Yan, Coupler-assisted controlled-phase gate with enhanced adiabaticity, Phys. Rev. Appl. **16,** 054020 (2021).

[23] P. Zhao, K. Linghu, Z. Li, P. Xu, R. Wang, G. Xue, Y. Jin, and H. Yu, Quantum crosstalk analysis for simultaneous gate operations on superconducting qubits, Phys. Rev. X Quantum **3,** 020301 (2022).

[24] R. Acharya, I. Aleiner, R. Allen, T. I. Andersen, M. Ansmann, F. Arute, K. Arya, A. Asfaw, J. Atalaya, R. Babbush *et al.*, Suppressing quantum errors by scaling a surface code logical qubit, Nature **614,** 676 (2023).

[25] S. Cao, B. Wu, F. Chen, M. Gong, Y. Wu, Y. Ye, C. Zha, H. Qian, C. Ying, S. Guo *et al.*, Generation of genuine entanglement up to 51 superconducting qubits, Nature **619,** 738 (2023).

[26] J. Koch, T. M. Yu, J. Gambetta, A. A. Houck, D. I. Schuster, J. Majer, A. Blais, M. H. Devoret, S. M. Girvin, and R. J. Schoelkopf, Charge-insensitive qubit design derived from the Cooper pair box, Phys. Rev. A **76,** 042319 (2007).

[27] P. Krantz, M. Kjaergaard, F. Yan, T. P. Orlando, S. Gustavsson, and W. D. Oliver, A quantum engineer's guide to superconducting qubits, Appl. Phys. Rev. **6,** 021318 (2019).

[28] ANSYS, Inc., ANSYS®Electromagnetics Suite, Release 2021 R2 https://ansys.com/academic/terms-and-conditions.

[29] H. Goto, Double-transmon coupler: Fast two-qubit gate with no residual coupling for highly detuned superconducting qubits, Phys. Rev. Appl. **18,** 034038 (2022).

[30] K. Kubo and H. Goto, Fast parametric two-qubit gate for highly detuned fixed-frequency superconducting qubits using a double-transmon coupler, Appl. Phys. Lett. **122,** 064001 (2023).

[31] D. L. Campbell, A. Kamal, L. Ranzani, M. Senatore, and M. D. LaHaye, Modular tunable coupler for superconducting circuits, Phys. Rev. Appl. **19,** 064043 (2023).

[32] R. Li, K. Kubo, Y. Ho, Z. Yan, Y. Nakamura, and H. Goto, Realization of high-fidelity CZ gate based on a double-transmon coupler, arXiv:2402.18926.

[33] J. M. Chow, S. J. Srinivasan, E. Magesan, A. D. Córcoles, D. W. Abraham, J. M. Gambetta, and M. Steffen, Characterizing a four-qubit planar lattice for arbitrary error detection, Proc. SPIE Int. Soc. Opt. Eng. **9500** (2015).

[34] Q. Zhu, S. Cao, F. Chen, M.-C. Chen, X. Chen, T.-H. Chung, H. Deng, Y. Du, D. Fan, M. Gong *et al.*, Quantum computational advantage via 60-qubit 24-cycle random circuit sampling, arXiv:2109.03494.

[35] X. Zhang *et al.*, Digital quantum simulation of Floquet symmetry-protected topological phases, Nature **607,** 468 (2022).

[36] D. M. Zajac, J. Stehlik, D. L. Underwood, T. Phung, J. Blair, S. Carnevale, D. Klaus, G. A. Keefe, A. Carniol, M. Kumph, M. Steffen, and O. E. Dial, Spectator errors in tunable coupling architectures, arXiv:2108.11221.

[37] M. Sarovar, T. Proctor, K. Rudinger, K. Young, E. Nielsen, and R. Blume-Kohout, Detecting crosstalk errors in quantum information processors, Quantum **4,** 321 (2020).

[38] L. H. Pedersen, N. M. Møller, and K. Mølmer, Fidelity of quantum operations, Phys. Lett. A **367,** 47 (2007).

[39] R. Kueng, D. M. Long, A. C. Doherty, and S. T. Flammia, Comparing experiments to the fault-tolerance threshold, Phys. Rev. Lett. **117,** 170502 (2016).

[40] M. Takita, A. D. Córcoles, E. Magesan, B. Abdo, M. Brink, A. Cross, J. M. Chow, and J. M. Gambetta, Demonstration of weight-four parity measurements in the surface code architecture, Phys. Rev. Lett. **117,** 210505 (2016).

[41] M. Takita, A. W. Cross, A. D. Córcoles, J. M. Chow, and J. M. Gambetta, Experimental demonstration of fault-tolerant state preparation with superconducting qubits, Phys. Rev. Lett. **119,** 180501 (2017).

[42] D. C. McKay, S. Sheldon, J. A. Smolin, J. M. Chow, and J. M. Gambetta, Three-qubit randomized benchmarking, Phys. Rev. Lett. **122,** 200502 (2019).

[43] N. Sundaresan, I. Lauer, E. Pritchett, E. Magesan, P. Jurcevic, and J. M. Gambetta, Reducing unitary and spectator errors in cross resonance with optimized rotary echoes, PRX Quantum **1,** 020318 (2020).

[44] S. Krinner, S. Lazar, A. Remm, C. K. Andersen, N. Lacroix, G. J. Norris, C. Hellings, M. Gabureac, C. Eichler, and A. Wallraff, Benchmarking coherent errors in controlled-phase gates due to spectator qubits, Phys. Rev. Appl. **14,** 024042 (2020).

[45] M. Malekakhlagh, E. Magesan, and D. C. McKay, First-principles analysis of cross-resonance gate operation, Phys. Rev. A **102,** 042605 (2020).

[46] T.-Q. Cai, X.-Y. Han, Y.-K. Wu, Y.-L. Ma, J.-H. Wang, Z.-L. Wang, H.-Y Zhang, H.-Y Wang, Y.-P. Song, and L.-M. Duan, Impact of spectators on a two-qubit gate in a tunable coupling superconducting circuit, Phys. Rev. Lett. **127,** 060505 (2021).

[47] J. R. Johansson, P. D. Nation, and F. Nori, QuTiP: An open-source python framework for the dynamics of open quantum systems, Comput. Phys. Commun. **183,** 1760 (2012).

[48] J. Johansson, P. Nation, and F. Nori, Qutip 2: A python framework for the dynamics of open quantum systems, Comput. Phys. Commun. **184,** 1234 (2013).

[49] P. Virtanen *et al.*, SciPy 1.0: Fundamental algorithms for scientific computing in PYTHON, Nat. Methods **17,** 261 (2020).

[50] J. M. Martinis and M. R. Geller, Fast adiabatic qubit gates using only $\sigma^z$ control, Phys. Rev. A **90,** 022307 (2014).

[51] F. Gerber, optimparallel-A parallel version of 'scipy.optimize.minimize(method='L-BFGS-B'), 2020, http://doi.org/10.5281/zenodo.3888570.

[52] F. Gerber and R. Furrer, optimParallel: An R package providing a parallel version of the L-BFGS-B optimization method, R J. **11,** 352 (2019).

[53] F. Motzoi, J. M. Gambetta, P. Rebentrost, and F. K. Wilhelm, Simple pulses for elimination of leakage in weakly nonlinear Qubits, Phys. Rev. Lett. **103,** 110501 (2009).